Reprinted from JOURNAL OF PHYSICAL OCEANOGRAPHY, Vol. 16, No. 7, July 1986
American Meteorological Society

Albedos and Glitter Patterns of a Wind-Roughened Sea Surface*

RUDOLPH W. PREISENDORFER AND CURTIS D. MOBLEY

Pacific Marine Environmental Laboratory/NOAA, Seattle, WA 98115-0070

(Manuscript received 9 October 1985, in final form 4 February 1986)

ABSTRACT

The downward albedo (irradiance reflectance) r_- and the upward albedo r_+ of a random air–water surface, formed by capillary waves, are computed as a function of lighting conditions and wind speed by Monte Carlo means for incident unpolarized radiant flux. The possibility of multiple scattering of light rays and of ray-shielding of waves by other waves is included in the calculations. The effects on $r_\pm$ of multiple scattering and wave shielding are found to be important for higher wind speeds ($\geq$10 m s^{-1}) and nearly horizontal light ray angles of incidence ($\geq$70°). The Monte Carlo procedure is used to generate reflected and transmitted glitter patterns as functions of wind speed and sun position. These results are used to check the procedure's patterns against observed patterns. A simple analytic first-order model of glitter patterns and irradiance reflectance, which assumes a binormal distribution of water facet slopes, is tested against the relatively exact Monte Carlo results. Regions are defined in wind-speed and incident-angle space over which the first-order model is acceptable. Plots of the Monte Carlo $r_\pm$ are drawn as functions of wind speed and angle of incidence of light rays. The albedos $r_\pm$ are also found for various continuous radiance distributions simulating overcast skies and upwelling submarine light fields just below the air–water surface. Good agreement is found, where comparison can be made, between the computed albedos and albedos measured over the ocean surface.

1. Introduction

In this study we develop a Monte Carlo procedure for estimating the unpolarized irradiance reflectance and glitter patterns of a wind-roughened sea surface as a function of environmental lighting conditions and wind speed, given the statistical properties of the surface. The procedure includes the effects of multiple scattering of light rays and their shielding by wave facets. Since the optical properties of the sea surface are determined primarily by capillary waves, even in the presence of gravity waves, our attention is directed mainly at the proper treatment of the capillary wave case. However, for completeness and possible future use, a model also has been developed which allows an exact calculation of the optical properties of a wind-roughened surface which has the form of a spatially stationary process over the full capillary–gravity range of water waves. This may be found in Preisendorfer and Mobley (1985), from which the present article has been condensed. (Hereafter, references to this work will be denoted by "PM.")

a. Some initial observations

To introduce the ideas below, we make the following observations.

1) THE AIR–WATER SURFACE AS A WIND-DRIVEN RADIOMETRIC VALVE

The amount of sunlight and skylight penetrating the surface of the sea generally increases as the surface becomes increasingly "crinkled" by gusts of wind. Moreover, this wind-induced increase of transmission is greater for rays of light coming in from near the horizon than for those arriving from near the zenith. These facts are made plausible by inspecting a plot of the Fresnel reflectance curve of a flat air–water surface as a function of the incidence angle for unpolarized light in the visible portion of the spectrum. For a narrow beam of unpolarized light, incident from the zenith on a flat air–water surface, nearly 98 percent of the beam's radiant flux penetrates into the sea below, whereas the beam incident at 80° from the zenith has only about 65 percent of its flux transmitted into the depths below. As a fresh breeze plays over the flat surface and crinkles it with capillary waves, the rays from the zenith now encounter tipped wave facets, which transmit a slightly smaller amount of light; however, these same water facets tipped toward the nearly horizontal incident rays allow a relatively greater light transmission. The net effect as we shall see below, according to Fresnel's law and the statistical form of the surface, is a greater overall transmission of radiant flux from sun and sky into the ruffled sea, relative to a flat, calm surface.

The sea surface thus acts as a wind-driven radiometric valve which allows greater or lesser amounts of radiant energy from the sky to penetrate the sea's upper

* Contribution No. 785 from NOAA/Pacific Marine Environmental Laboratory.

layers, in accordance with wind speed and lighting conditions over the surface. The net effect of increased light transmission from the sky and sun is to warm the near-surface water, to drive photosynthesis, and eventually to help power the basic elements of both the climate and life of planet Earth (e.g., Duntley, 1963).

2) Reflectances as initial conditions in hydrologic optics

A mathematical means by which the climatic and other matters in subsection 1 can be explored is the set of solutions of the irradiance differential equations for the light fields in lakes and seas. As shown in Preisendorfer and Mobley (1984), the light field in an optically deep hydrosol, such as a sea, is determinable once the downward irradiance reflectance (albedo) r_- and upward irradiance reflectance r_+ of the random sea surface are known along with the depth dependence of the sea's optical properties. In this work we show how to obtain the albedos $r_\pm$ for a randomly capillaried sea or lake surface with given wind speed and lighting conditions over it. The quantities $r_\pm$ may then serve as initial conditions in the solution of the irradiance equations by properly accounting for the optical properties of the wind-roughened air–water surface. From the depth-variation of the irradiance field, the potential heating of the upper water layers may be determined using the wavelength-dependent volume absorption function in those layers.

3) A first-order analytic ray-tracing theory

The problem of estimating the reflectance and transmittance of a wind-roughened sea surface using analytic methods is relatively simple when the wind speed is small so that the air–water surface is only mildly rippled. As we shall see below, a simple first-order (single-scatter) analytic theory adequately describes the glitter pattern and hence reflectance properties of the sea surface for sufficiently low wind speeds and for light rays incident on the surface from sufficiently near the zenith (e.g., for winds of less than 5 m s^{-1} when the angle of incidence is within 60° of the zenith).

4) Effects of multiple scattering and shielding of rays

When the wind speeds become too great or when rays of light are incident on the water from nearly horizontal directions, the first-order analytic theory is no longer statistically acceptable because the light rays are more likely to undergo multiple scattering among the wave facets. There is also a shielding effect of one wave facet blocking rays from getting to another facet, which the first-order theory does not handle. We find that the effect of multiple scattering of light rays is to slightly decrease the net penetration of sunlight and skylight into the sea or, alternately, to increase r_-, since there are repeated opportunities for the sea surface to reflect the (usually near-grazing) radiant flux of a multiply reflected incident ray back into the sky above. On the other hand, the shielding action of a facet tends on average to increase the amount of light penetrating the surface because the intercepting facets on average tilt their normals toward the line of approach of the incoming ray.

The net effect of multiple scattering and shielding (relative to single-scattering estimates) is small and amounts, for example, to about a 2 or 3 percent increase in the sea surface irradiance reflectance for wind speeds around 10 m s^{-1} and individual angles of ray incidence around 80° from the zenith; for these conditions the irradiance reflectance is on the order of 0.20. The practical effect of this on solar irradiance estimates is relatively small. For example, the solar irradiance over the visible spectrum (400–700 nm) at sea level in moist air, with the sun near the horizon at 80° from the zenith, on an otherwise clear day amounts to about 75 W m^{-2}. Of this, about 0.20×75, or 15 W m^{-2}, are reflected. Hence, inclusion of multiply scattered radiant flux in the sun- and sky-reflected flux estimates will, in this example, increase the estimates (relative to single-scatter estimates) at most on the order of $0.03 \times 15 = 0.5$ W m^{-2} at each point of the sea over its sunlit expanse at low sun altitudes (as in the polar regions of the earth). This increase is small relative to our estimates of the decrease of downward reflectance of the sea when the wind speed ranges from 0 to 20 m s^{-1}. Over this wind speed range, the averaged surface reflectance for sun rays incident at 80° from the zenith drops from about 0.35 at 0 m s^{-1} (with 26 W m^{-2} reflected) to 0.17 at 20 m s^{-1} (with 13 W m^{-2} reflected), i.e., by about a factor of 2.

5) Alongwind and crosswind effects on transmittance

There is another small but calculable effect on the transfer of light downward past the windblown sea surface that on average is also on the order of magnitude of the multiple-scatter and shielding effects. Experiments show (Preisendorfer, 1976, Vol. VI, pp. 145–151) that the normals to the capillary wave facets in the alongwind vertical plane tend on average to be tipped away from the vertical at greater angles than those in the crosswind vertical plane. Hence, light rays, at a fixed zenith angle, incident on the rippled sea surface in the alongwind plane on average undergo a greater transmission into the sea compared to those incident in the crosswind plane. The difference in r_- for these two modes of incidence is on the order of 5 percent for wind speeds around 10 m s^{-1} and angles of incidence around 80° from the zenith.

b. Historical notes

An early important investigation of the optical properties of the sea surface is reported in Hulburt (1934). The modern experimental study of optical effects of water waves begins in the work of Duntley (1950) where direct in situ electronic measurements of the capillary water-wave slopes were made using two pairs of parallel, vertical, immersed wires. One pair formed a plane in the alongwind direction and the other a plane in the crosswind direction. (See Preisendorfer, 1976, Vol. VI, p. 138. Henceforth, bibliographic references to this work will be abbreviated as, e.g., "*H.O.* Vol. VI, p. 138.") Initial analytical consequences of Duntley's research, for radiative transfer across a random air–water surface, are drawn in Duntley and Preisendorfer (1952). In particular, it was found that the wave slopes ζ_u and ζ_c in the alongwind and crosswind directions are normally distributed, independent variates. The wave-slope/wind-speed laws deduced from these studies, showing variance of the alongwind and crosswind wave slopes proportional to wind speed—a main building block in the present article—are recorded in Duntley (1954). An alternate optical approach to water-surface geometry may be found in Schooley (1954). About this time the research of Cox and Munk in which the inverse problem was solved (1954a,b, 1955) was completed: from photographs of remotely observed sun glitter patterns, the statistical properties of the sea surface were deduced. To effect this solution, Cox and Munk used an ingenious geometric analysis of the glitter pattern photographs, completing a project which, in Hulburt's (1934) view, was regarded as a difficult task (cf. *H.O.*, Vol. VI, p. 138). The main result again showed that (ζ_u, ζ_c) is a pair of independent, normally distributed variables whose variances increase linearly with wind speed.

In an important sense the experimental works of Duntley and of Cox and Munk are dual and complementary: Duntley in effect placed his wave slope meter at a fixed point in the sea and made long-time observations of the alongwind and crosswind wave slopes there; the Cox and Munk aerial photographs were made at a fixed instant in time and cover a wide spatial expanse of sea. When comparing the wave-slope/wind-speed laws deduced by Cox and Munk (1954a) and by Duntley (1954), we see that ergodic equivalence reasonably holds for these dual forms of sea surface statistics (cf. *H.O.* Vol. VI, pp. 148–151). That is, for the conditions of their experiments, time-averaged wave slope statistics at a point and space-averaged wave slope statistics at an instant are sensibly equal. This provides the basis for the stationary random-surface approaches to the sea surface reflectance problem followed in the present study (cf. PM).

Another important empirical law needed for a thorough study of the reflectance problem of wind-roughened seas was implicitly found by Neumann (1953) at about the same time that Duntley, and Cox and Munk were doing their experiments. This is the wave-elevation/wind-speed law showing that the variance of gravity wave elevation in a statistically stationary sea is proportional to the fifth power of wind speed. Neumann's work was generally concurrent with and inspired by the researches of Pierson (1955) and Pierson and Marks (1952), who contributed to our modern representations of the random sea surface by using novel stochastic integration techniques. For a derivation of the Neumann spectrum, the wave-elevation/wind-speed law, and the relation of the Neumann spectrum to subsequent water wave spectra, see *H.O.*, Vol. VI, pp. 181–194. In PM we use the Neumann spectrum and its modern generalizations to lay the groundwork for an exact Monte Carlo procedure to determine the reflectance and transmittance of a statistically stationary random wind-aroused sea surface consisting of superpositions of wave trains ranging from capillary ripples to long gravity swells.

A recent Monte Carlo study of sun glitter patterns, as well as references to earlier glitter studies by the same authors and their colleagues, may be found in Guinn et al. (1979). The capillary slope statistics of Duntley and of Cox and Munk are used in these calculations. We shall build on this important series of studies by looking specifically at the glitter and reflectance problem using a capillary-wave model that incorporates multiple scattering of light rays and the shielding of wave facets, as discussed in section 1a. We note in passing that some analytical attempts at solving the reflectance problem for wind-roughened seas have been made (cf. *H.O.*, Vol. VI, footnote 8, p. xii; *H.O.*, Vol. VI, sections 12.10–12.14; and Preisendorfer, 1971).

2. Computational procedure

The present computations leading to the desired optical properties of the wind-roughened sea surface fall into four main stages:

(i) construction of a realization of the random air–water surface,
(ii) tracing incident parent light rays over, under, and through the realized surface toward their ultimate destinations,
(iii) assigning radiant flux content to each processed daughter ray, and
(iv) stacking daughter rays (that proliferate by multiple scattering of the parent ray) to await further processing, as in (ii) and (iii).

The steps needed to implement these four main stages now will be described in sufficient detail for a basic understanding of the computational procedure. Slightly more detail will be given in the following sections; however, a reader wishing to generate a program

of these four stages should consult PM, where statistical, geometrical, and physical details are given.

Figure 1 shows a perspective view of part of the water surface and a multiply scattered ray. A finite region of the mean water surface is resolved by a hexagonal grid of triangles. At each triangle vertex the sea surface elevation is defined, so that the waves are represented by a set of triangular facets. These facets are contained in the hexagonal domain (the cylindrical region of space) defined by the hexagonal grid. Four such facets are shown in Fig. 1. After a particular surface realization has been generated in stage (i), a light ray of unit radiant flux is aimed toward the surface from any chosen direction. Figure 1 shows such a ray entering the hexagonal domain at point A. Every such initial ray eventually strikes a surface wave facet, as at B. In general, each encounter of a ray with a wave facet generates both a reflected and a refracted daughter ray. The directions and radiant flux contents of these daughter rays are determined by Snell's law and Fresnel's formula, respectively. The daughter rays may undergo further encounters with other wave facets. As illustrated in Fig. 1, the first refracted ray at B, heading downward through the water, leaves the hexagonal domain at D without further scattering. The first reflected ray at B, however, intercepts another facet at C, generating two more rays. The reflected ray starting from C leaves the domain at E. The refracted ray starting from C encounters yet another facet at F and undergoes a total internal reflection before leaving the domain at G. Thus, the initial ray finally results in one reflected and two refracted rays emerging from the hexagonal domain. The fluxes at the points of emergence contribute to the appropriate reflectance and transmittance calculations.

Figure 2 gives an overview of the computational process in the form of a flow diagram of eleven steps. In step 1 of the diagram the computer run is initialized by choosing the wind speed and direction, size of the hexagonal grid, lighting conditions, and the like. In step 2 a realization of the random surface is constructed over the hexagonal grid. In step 3 an initial ray incident along the desired direction ξ' is specified. This *parent ray* may approach the surface from the air side, as ray AB in Fig. 1, or from the water side. The parent ray ξ' is assigned a radiant flux $P' = 1$, and the point $\mathbf{p}'$ where the ray enters the hexagonal domain (e.g., point A of Fig. 1) is determined. The information $(\xi', \mathbf{p}', P')$, which fully determines a ray, is then stored in an array S, called the *stack*. (S in practice has dimensions of 10×7. The seven-dimension part of S holds the components of the vectors ξ' and $\mathbf{p}'$, and the scalar P'. The ten-dimension part of S allows for up to ten rays to be queued at any one time. Never in our experience with the model were as many as ten rays in the stack simultaneously.) In step 4 we pull the next available ray triple $(\xi, \mathbf{p}, P)$ from the stack and trace the ray to completion in step 5. That is, in step 5, we prolong the ray from $\mathbf{p}$ along direction ξ until either the surface is encountered or the ray leaves the hexagonal domain. If, in executing step 5, the surface is encountered, the point $\mathbf{p}_i$ of interception of the ray and the surface is determined (e.g., point B in Fig. 1) and *daughter rays* (e.g., BC, BD in Fig. 1) are produced. In step 6, one daughter ray is always generated at $\mathbf{p}_i$ along the reflected direction ξ_r. In step 7, one daughter ray will be generated along the transmitted direction ξ_t if and only if the parent ray is not totally internally reflected at $\mathbf{p}_i$. (For example, at point F in Fig. 1, total internal reflection takes place and there is no transmitted daughter ray.) In either of

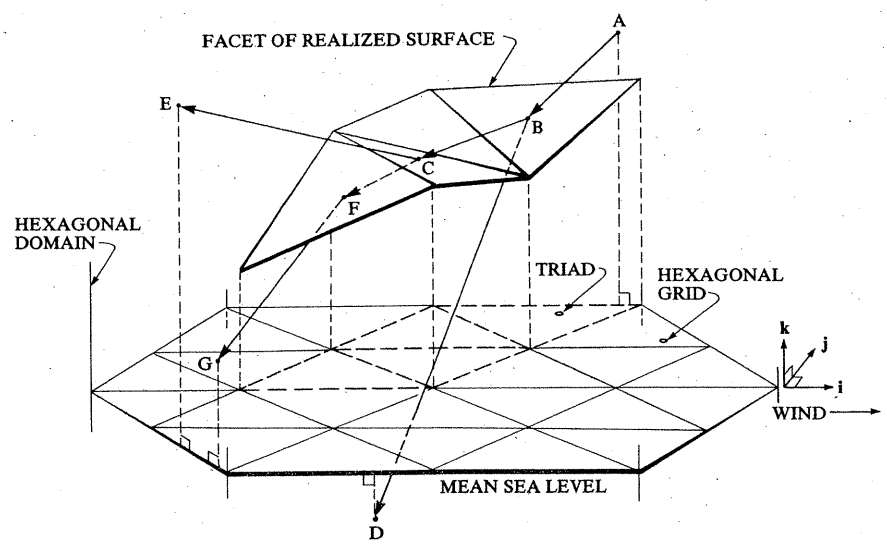

FIG. 1. Illustration of the hexagonal domain with a particular surface realization and ray tracing. Observe the orientation of the horizontal triangular facets (triads) relative to the downwind direction.

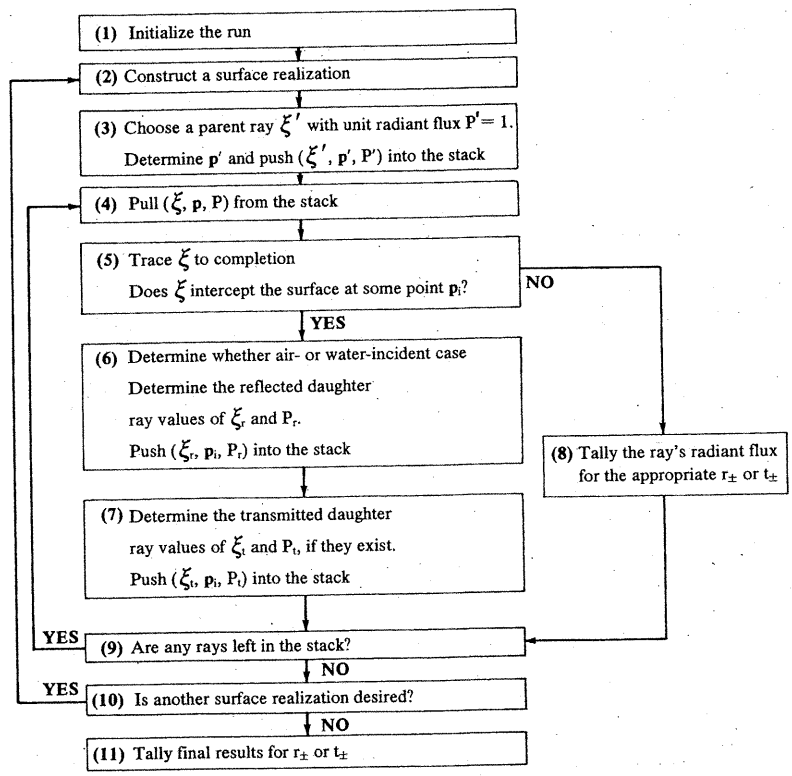

FIG. 2. Ray-tracing flow diagram.

steps 6 or 7, the direction ξ of the parent ray (which of course may be a daughter ray from a previous ray–surface interception), the normal $\mathbf{n}$ to the intercepted wave facet, and the daughter ray direction ξ_r determine an associated Fresnel factor for reflectance. This factor is multiplied into the current radiant flux P of the parent ray to obtain the flux content P_r of the reflected daughter ray. The flux content of the transmitted ray is then $P_t = P - P_r$. The daughter ray triples are pushed into the stack for further processing. On the other hand, step 5 may fail to produce a point of interception $\mathbf{p}_i$ (as at D, G, E of Fig. 1) in which case the ray has finished its interactions with the surface in the hexagonal domain and its radiant flux content is added (in step 8) to an accumulating sum for the irradiance reflectances r_+ or r_- as the case may be.

In practice an initial parent ray may go on to encounter the air–water surface a large number (~ 10) of times so that, at some stage in the running calculation, several of its daughter ray triples may be simultaneously in the stack awaiting further processing of the kind in step 5 (during which processing they, in turn, can generate more daughter ray triples). The pushing activity of steps 3, 6 and 7 places each ray triple in the stack as soon as the ray is generated. The stack is systematically serviced by the pulling activity of step 4 via step 9. The stack is crucial to the ray-tracing algorithm, since it allows the "tree" of multiply scattered rays to grow without restrictions on the number of ray–surface interactions or upon the order in which daughter rays are traced to completion. When the stack of waiting ray triples is depleted, we check in step 10 to see if another surface realization is needed. If so, we return to step 2 of the ray-tracing flow diagram and begin anew; otherwise the final results are computed in step 11.

In the work below we routinely use 2000 or more surface realizations for each fixed initial incident direction ξ'. If the initial parent ray is air-incident, then the calculation results in the downward reflectance r_-. If the initial parent ray is water-incident, we obtain r_+. In this way, using ample numbers of realized surfaces, we can build up the statistics r_+ and r_- with controllably small variances about their "true" values. Transmittances $t_\pm$ are obtained from the final $r_\pm$ values via $t_\pm = 1 - r_\pm$.

3. Constructing capillary wave surfaces

Step (i) of the computational procedure of section 2 will now be outlined.

In the historical notes of the introduction, it was observed that the statistics of the capillary wave structure of the sea surface reside in the wave-slope/wind-speed laws. We use these statistics to construct realizations of the random capillary wave surfaces. Let σ_u^2 and σ_c^2, respectively, be the (dimensionless) upwind and crosswind variances of the independent, normally

distributed capillary wave slopes ζ_u and ζ_c at a point. Then (*H.O.*, Vol. VI, p. 145) the general forms linking these variances and the wind speed U are

$$\sigma_u^2 = a_u U$$
$$\sigma_c^2 = a_c U, \tag{1}$$

where

$$a_u = 3.16 \times 10^{-3} \text{ s m}^{-1}$$
$$a_c = 1.92 \times 10^{-3} \text{ s m}^{-1}, \tag{2}$$

and where U is in meters per second measured at a height of 12.5 m above mean sea level.

Let σ_ζ^2 (in meters^2) be the variance of the normally distributed capillary wave elevation ζ at a point. The wave-elevation/wind-speed law for capillary waves is assumed to be generally of the form

$$\sigma_\zeta^2 = a_\zeta U^q. \tag{3}$$

It turns out that we can model the random capillary surface without having to explicitly determine a_ζ and q (cf. PM for details). Briefly, suppose that the along-wind and crosswind dimensions of the triads in Fig. 1 are, respectively, δ and ϵ. Let the three ordinates of each of the wave facets in Fig. 1 be randomly and independently drawn from a normal population of zero mean and variance σ^2, and let ζ be the elevation of a facet centroid. Then $\sigma_\zeta^2 = \sigma^2/3$. Analysis shows that with (1) and (3) in force, $\epsilon^2/\delta^2 = 3a_u/4a_c$, and so the shape of a triad is independent of wind speed and of the physical dimensions of δ and ϵ. We may then set $\delta = 1$, a dimensionless unit. The parameters σ, δ and ϵ are thereby fixed and dimensionless, and turn out to be

$$\delta = 1$$
$$\epsilon = [3a_u/4a_c]^{1/2}$$
$$\sigma = [(a_u/2)U]^{1/2}. \tag{4}$$

The *random capillary surface* associated with a wind speed U is a set of realizations constructed as follows. Build a hexagonal grid as in Fig. 1 with triads of dimensions δ, ϵ, as given in (4). At each vertex of a triad in the hexagonal grid, randomly and independently draw samples from $N(0, \sigma^2)$, the normal population of zero mean and variance σ^2 as computed from (4), and erect ordinates with these sample values. Thus over (or under) each triad there is constructed a *facet*. The surface formed by such a set of facets constitutes one realization of the random capillary surface.

With these constructions it can be seen (cf. PM) that the upwind and crosswind slopes ζ_u and ζ_c of the set of facets on the realized surface follow the probability density function

$$p(\zeta_u, \zeta_c) = (2\pi\sigma_u\sigma_c)^{-1} \exp\left[-\frac{1}{2}\left(\frac{\zeta_u^2}{\sigma_u^2} + \frac{\zeta_c^2}{\sigma_c^2}\right)\right], \tag{5}$$

where σ_u^2 and σ_c^2 are given by (1). Thus a random surface built over the hexagonal grid of Fig. 1 in the manner just described will obey the classic wave-slope/wind-speed law of capillary waves. Moreover, the dimensionless horizontal (δ, ϵ) and vertical (σ) scales of such a surface, for each fixed choice of U, will permit the correct modeling of wave shielding and multiple scattering of light rays. Implicit here is the assumption that in real life, as in the model, the various numerical attributes (elevation, slope, etc.) of the wave facets in nonadjacent triads are independent random variables. At present the spatial autocorrelation property of a random capillary surface is not known. The present model can be modifed when such additional information is available.

4. Ray tracing

The ray tracing step (ii) of section 2 takes the form of a sequence of problems in analytical geometry and plane-surface optics. The solution procedure implemented in PM begins by projecting the light ray being traced (e.g., the reflected ray emanating from point B in Fig. 1) onto the horizontal hexagonal grid of triads to form the *track* of the ray. This track of the light ray is then extended to the boundary of the hexagonal grid. A ray track, in general, crosses many triads of the hexagonal grid before the boundary is reached. These ray track–triad intersections allow the identification of those associated wave facets which are candidates for intersection with the light ray. Using simple geometry for finding the intersection of a line and a plane, where now the line is the light ray and the plane is that of the triangular wave facet, we systematically check the candidate wave facets for a ray–facet intersection. For example in Fig. 1, the reflected ray from B passes over one wave facet before intercepting the next facet at C. If the ray being traced intercepts a wave facet before the hexagonal grid boundary is reached, then the incident ray direction and the direction of the normal to the intercepted facet allow us to apply the law of reflection of rays and Snell's law of refraction and thus determine the directions of the reflected and transmitted (if any) daughter rays.

Every time a ray intercepts a facet, the radiant flux content of the ray is split into two parts assigned to its daughter rays by means of the Fresnel reflectance and transmittance factors for unpolarized flux. The solution of the above intersection problem yields the angles of reflection and refraction of a ray on a facet needed to evaluate the Fresnel factors. The full implementation of these simple physical insights requires about twenty pages of algebraic development, in PM, before all cases are considered and described in sufficient detail to allow programming.

5. Defining albedos

The irradiance reflectance (or albedo) of a random air–water surface is the ensemble average, over the set of realized surfaces, of many individual ray reflectances.

Figure 3 shows two cases of a portion of the ωth realization of the air–water surface being encountered by an incident ray ξ' arriving from the air. The upper panel of this figure is for the case of single scattering, and the lower panel illustrates the multiple scattering case. We place an imaginary horizontal monitoring surface (hms), of upward normal $\mathbf{k}$, at any convenient height above the hexagonal grid. The incident ray ξ' is the center of a bundle of rays of small solid angle $\Delta\Omega$ and small cross-section area ΔA normal to ξ'. This bundle has radiance $N(\xi')$ and intercepts the hms over patch I which has area $\Delta A/|\xi' \cdot \mathbf{k}|$. The bundle in the upper panel of Fig. 3 goes on to intercept the air–water surface in patch A with normal $\mathbf{n}$. There the bundle is reflected upward along ξ and emerges from the hms through patch R. If $P(\mathrm{I})$ $(=N(\xi')\Delta A\Delta\Omega)$ and $P(\mathrm{R};\omega)$ are the radiant fluxes through these patches, then by Fresnel's reflection coefficient $r(\xi' \cdot \mathbf{n})$ we have the following one-sample estimate of the albedo of the surface:

$$r_-(\xi';\omega) \equiv P(\mathrm{R};\omega)/P(\mathrm{I}) = r(\xi' \cdot \mathbf{n}).$$

In general, if $P(\mathrm{R};\omega)$ is the radiant flux emerging from patch R of the hms after one or several interactions with the ωth surface realization when flux of amount $P(\mathrm{I})$ is initially incident to the hms over patch I, then we set

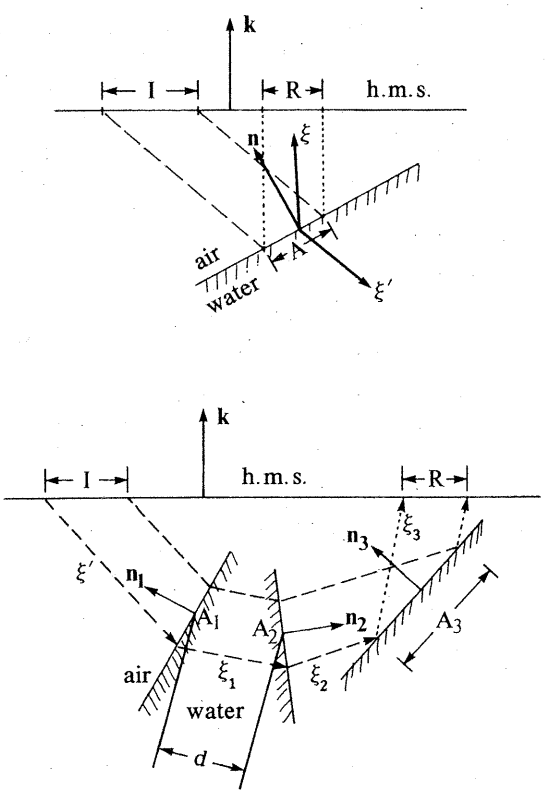

FIG. 3. Use of the horizontal monitoring surface (hms) for the single scattering (upper panel) and multiple scattering (lower panel) cases.

$$r_-(\xi') \equiv \frac{E_\omega P(\mathrm{R};\omega)/[\Delta A/|\xi' \cdot \mathbf{k}|]}{N(\xi')\Delta\Omega|\xi' \cdot \mathbf{k}|} \equiv E_\omega r_-(\xi';\omega) \tag{6}$$

where E_ω is the ensemble average operator and $r_-(\xi';\omega)$ is the product of all the Fresnel reflectances $r(\xi_j \cdot \mathbf{n}_k)$ or transmittances $[1 - r(\xi_j \cdot \mathbf{n}_k)]$ encountered along the way through the ωth realization from patch I to patch R (as in the lower panel of Fig. 3). In various cases studied, $r_-(\xi';\omega)$ also included exponential factors of the form $\exp[-\alpha d]$, where α is the volume attenuation coefficient for the water and d is the distance the ray travels through the water, as shown in the lower panel of Fig. 3. Setting $\alpha = 0$ makes the water transparent; setting $\alpha = \infty$ in effect eliminates any multiple scattering arising from subsurface travels of daughter rays. The factors making up the terms $r_-(\xi')$ are accumulated recursively via P_r and P_t during the execution of steps 6 and 7 in Fig. 2.

The purpose of (6) is to show that $r_-(\xi')$, so obtained, is an *irradiance* reflectance, i.e., the ratio of a *radiant emittance* in the numerator of (6) to an incident *irradiance* in the denominator. Recall that $\Delta A/|\xi' \cdot \mathbf{k}|$ is the area of patch I; this is the area that must be assigned to the ensemble average of the emergent radiant fluxes. When multiplied into the incident irradiance $N(\xi')\Delta\Omega|\xi' \cdot \mathbf{k}|$, $r_-(\xi')$ gives the ensemble-averaged radiant emittance of the hms. This average radiant emittance may clearly be associated to the mean sea level surface, since the absolute elevation of the hms was arbitrary during the derivation of (6).

6. Multiple scattering

A phenomenon which is difficult to handle in analytic formulations, but nearly trivial in the present numerical study, is that of multiple scattering. We define the *scattering order* (n_s) as the total number of times a parent ray or any of its daughter rays intercepts the wave surface. The *branch number* (n_b) is the total number of rays which occur in the scattering event. For initial light rays which approach the air–water surface from the air side, termed *air-incident* rays, the three-branch, single scattering event, shown schematically in the upper left panel of Fig. 4, is by far the most common at all wind speeds and angles of incidence. As the wind speed increases, or if incident rays come in nearly horizontal, then the scattering orders and branch numbers increase. Of the many possible configurations for air-incident multiple scattering, the second-order scatter, five-branch case is the most common, with third-order scatter, seven-branch cases being the next most common. Configurations such as $n_s = 3$, $n_b = 6$ (the case shown in Fig. 1) are rare, and cases where $n_b \geq 10$ almost never occur. For initial rays approaching the air–water surface from the water side, termed *water-incident* rays, single scattering events are also most common. The bottom row of Fig. 4 shows how these

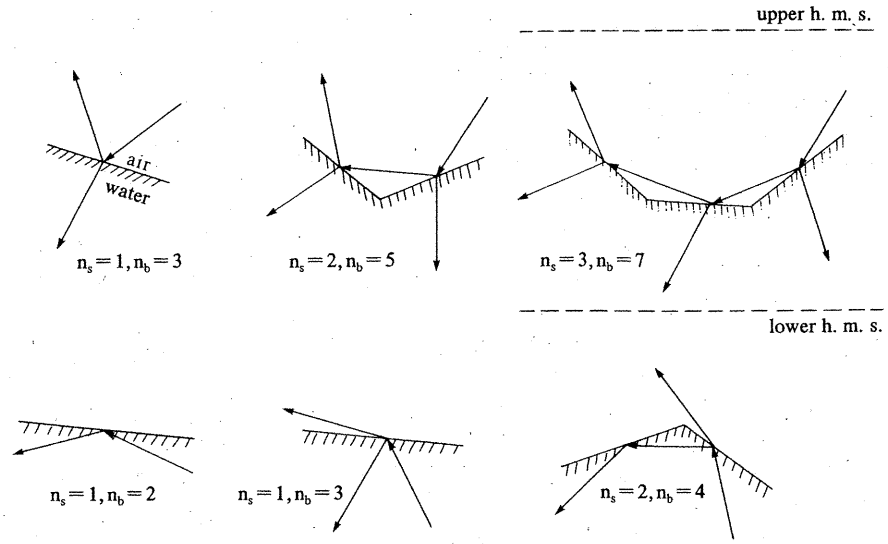

FIG. 4. Schematic diagrams of common scattering events. The top row is for the air-incident case; the bottom row is for the water-incident case. n_s counts the number of ray–surface encounters, n_b the total number of parent and daughter rays (branches).

single scattering events consist of two kinds: the case of $n_s = 1$, $n_b = 2$, when total internal scattering occurs and the case of $n_s = 1$, $n_b = 3$, when an upward transmitted ray occurs. For crinkly surfaces, water-incident rays can undergo multiple scattering ($n_s \geq 2$), as indicated in the $n_s = 2$, $n_b = 4$ case of Fig. 4.

Figure 5 shows how multiple scattering of rays depends on wind speed and angle of incidence of the parent light rays. For purposes of labeling graphs such as Fig. 5, it is convenient to define the incident angle θ'_s as the acute angle between the light source and either the zenith direction (for air-incident rays) or the nadir direction (for water-incident rays). Then $0 \leq \theta'_s \leq 90°$, and the phrase "air-incident rays" or "water-incident rays" must be added to avoid ambiguity. Figure 5 shows, as a function of θ'_s and wind speed, the percentage of incoming rays which undergo multiple scattering of any order ($n_s \geq 2$). This figure is for incoming rays which are parallel to the wind direction. The figure is based on over 150 000 ray tracings. The curves are applicable to both air-incident and water-incident rays. Observe that, for a given incidence angle θ'_s, the percentage of rays undergoing multiple scattering generally increases with wind speed U (except for the incident angle range between 80° and 90°). Rays incident from within 30° of the zenith or from a similar cone near the nadir almost never have multiple scatters for winds in the range $U = 0$ to 20 m s^{-1}. We see that for wind speed $U \geq 5$ m s^{-1}, typically five to ten percent of the rays incident from the range $60° \leq \theta'_s \leq 80°$ have multiple scatters. This is because the relative angles between the tilted wave facets and the incident rays are then most conducive to reflecting the incident ray into a nearly horizontal direction, so that the reflected daughter ray hits a neighboring facet. There is an overall dropoff in multiple scattering with increasing windspeed for nearly horizontal (80°) incoming rays, since the daughter rays then tend to head away from the surface at angles which cause them on average to miss even the nearest facets. We note as a general rule that around 10 percent of the rays undergo multiple scattering by capillary waves over a wide range of incident angles and wind speeds. The quantitative effects of multiple scattering will be discussed at appropriate locations below.

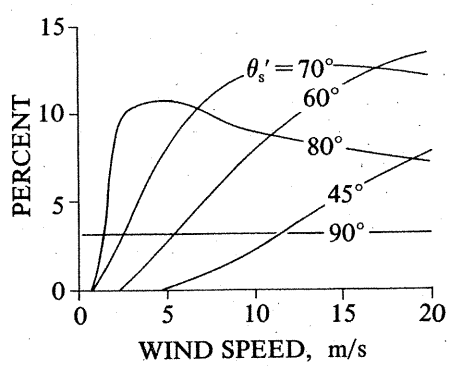

FIG. 5. The percentage of incident rays as a function of wind speed, which undergo multiple scattering, for capillary waves with incident rays parallel to the wind ($\phi'_s = 0°$).

7. Glitter patterns

The reflected glitter patterns formed by sun or moonlight on a wind-roughened water surface are a visually interesting manifestation of the random nature of the surface. We produced glitter patterns as a matter

of course in the present study leading to the required surface albedos. By comparing the Monte Carlo simulations of the glitter patterns with real counterparts, an impression of the skill of the simulation procedure could be gained. We summarize here only a small aspect of the glitter pattern analyses recorded in PM, mainly to indicate the realistic results attainable by the present procedure and to prepare the way for the evaluation of the first-order analytic glitter pattern theory noted below.

Figure 6 is the geometric setting for a glitter pattern representation. Imagine the sea to be flat calm. Let a ray ξ' from the sun's center arrive at point S of the mean sea level surface. Set up an **x**–**y**–**z** coordinate frame with orthonormal vectors **x**, **y**, **z**, such that ξ' is in the vertical **x**–**z** plane and such that $\xi' \cdot \mathbf{x} > 0$. The ray ξ' is reflected in the horizontal surface at S and moves along the specular reflection direction **a**. At a distance f along **a** from S we set up at point P a plane perpendicular to **a**. An orthonormal reference frame for this plane is established by defining a *horizontal* unit vector $\mathbf{h} \equiv -\mathbf{y}$ and a *vertical* unit vector $\mathbf{v} \equiv \mathbf{a} \times \mathbf{h}$. A finite rectangular subset of this plane is defined by choosing the two bounding angles ψ_h and ψ_v as shown in Fig. 6, and we call this finite subset the *image plane.* The image plane simulates the film in a camera and serves to represent a glitter pattern photograph when turned "upside down" for viewing, as suggested by the "top," . . . , "bottom" designations around its rim. When viewed as a photograph, **h** and **v** are appropriate horizontal and vertical axes. The *viewing angles* ψ_h and ψ_v are defined with $\psi_h > 0$ to the right of the *specular point* P in the photograph and with $\psi_v > 0$ above the specular point. The viewing angles, when displayed on a glitter pattern photograph, give the observer a feeling for the angular extent of the pattern as it would be seen from an airplane, for example.

Now replace the mean sea level plane in turn by successive realizations of a random sea surface. As ξ' is reflected in each realization, it produces an associated ray ξ which meets the image plane at some point **t**. The set of all such **t**-points produced in the image plane, by going through the ensemble of realizations, is the associated *glitter pattern.* The reference PM gives simple analytical relations between the glitter point locations $\mathbf{t} = (t_h, t_v)$ in the image plane and the viewing angles (ψ_h, ψ_v).

The inset in Fig. 6 shows the general relation between the *sun-based* **x**–**y**–**z** frame of current interest and the *wind-based* **i**–**j**–**k** frame of Fig. 1. The two coordinate systems share the same vertical direction, namely $\mathbf{z} = \mathbf{k}$. The unit vector ξ' describing a photon path (the direction of photon motion) has the representation $\xi' = (\sin\theta' \cos\phi', \sin\theta' \sin\phi', \cos\theta')$ in the wind-based **i**–**j**–**k** system, where $0° \leq \theta' \leq 180°$, $0 \leq \phi' \leq 360°$, and ϕ' is measured positive counterclockwise from **i**. As was remarked in the discussion of Fig. 5, it is also convenient to use the wind-based light source *location angles* θ'_s and ϕ'_s which point toward the sun or general point source, as shown in Fig. 6. We have the general connections $\theta'_s = 180° - \theta'$, and $\phi'_s = 180° + \phi'$ (modulo 360°), so that if $\xi'_s = (\sin\theta'_s \cos\phi'_s, \sin\theta'_s \sin\phi'_s, \cos\theta'_s)$ is the unit vector pointing toward the sun, we have $\xi'_s = -\xi'$.

In our Monte Carlo calculations we use the wind-based system, owing to the simplicity of the probability

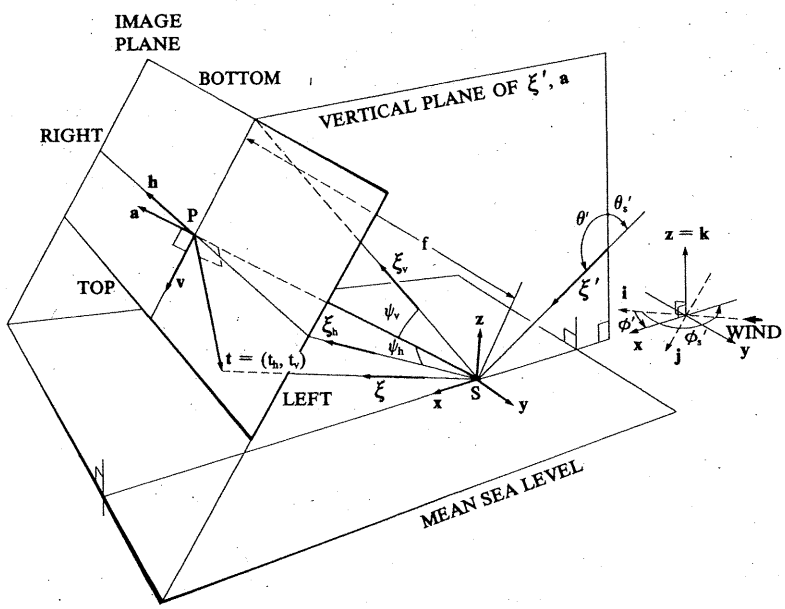

FIG. 6. Sun-based **x**–**y**–**z** coordinate system used in defining the image plane by simulating a photograph of the glitter pattern on the water surface.

distribution (5) in that system (ζ_u and ζ_c are uncorrelated there). However, it is more natural to depict glitter patterns in the sun-based system using the image plane of Fig. 6. Each coordinate system is the logical one for its purpose, and little effort is required to switch between them, since they are related by a rotation about their common vertical axes.

The situation depicted in Fig. 6 is one of four general orientations of the camera-like image plane. Figure 7 shows all four camera positions used to present glitter patterns. Camera A photographs air-incident reflected rays, the usual case of the sun's glitter on the sea surface, and corresponds to Fig. 6. The camera angle θ_c is θ'_s, the angle of reflection for a level surface. Camera B, located along the specular transmission ray path, photographs the glitter pattern of air-incident transmitted rays as the pattern would be seen, for example, by a scuba diver looking upward. The camera angle is $\theta_c = \arcsin(m^{-1} \sin\theta'_s)$, the angle of refraction for a flat horizontal water surface. Here m is the index of refraction of the water, to which we give the value $m = 4/3$, a good approximation over the visible spectrum. Cameras C and D photograph the reflected and refracted glitter patterns, respectively, for an underwater light source. As remarked in section 6 and as seen in Fig. 7, the angle of incidence θ'_s for water-incident rays is often measured from the nadir. If the underwater light source is positioned so that there would be no transmitted rays for a calm surface, the camera D axis is placed in the specular (mean) water surface ($\theta_c = 90°$).

Associated with each glitter point **t** in the image plane is a pair of angles (α, β), introduced by Cox and Munk (1954a), which define the orientation of the normal **n** to the water-surface facet producing the glitter point. If $\mathbf{n} = (n_x, n_y, n_z)$ in the sun-based frame, then

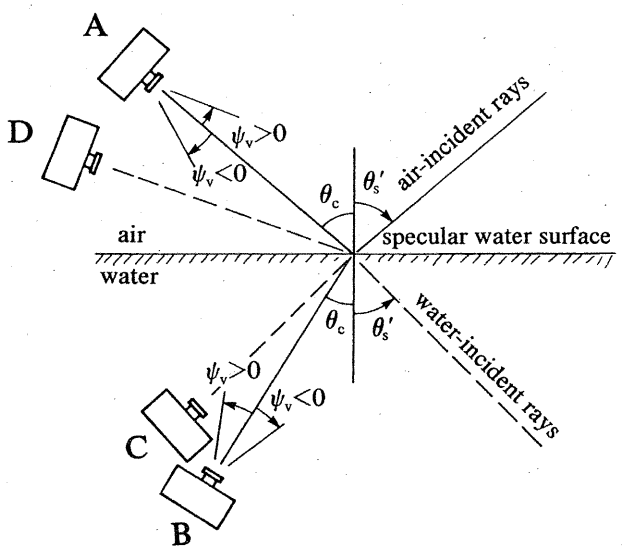

FIG. 7. Camera positions for viewing the four types of glitter patterns.

$$\alpha = \arctan(-n_y/n_x)$$

$$\beta = \arccos(n_z).$$

Thus β is the angle of tilt of **n** from the vertical, and the azimuth angle α of **n**'s projection on the horizontal plane is measured positive clockwise from the **x**-axis in Fig. 6. Conversely, from an (α, β) reading in the glitter diagram, we can reconstruct **n**. Details of these connections are given in PM. Contours of the azimuth and tilt angles displayed on a glitter pattern thus give the viewer a feeling for how much the water facets depart from the level, specular surface.

Figure 8 shows two Monte Carlo generated air-incident, reflected glitter patterns. The image plane orientation is therefore that of Fig. 6, or of camera location A in Fig. 7. There are 2000 points each for a wind of $U = 5$ m s^{-1}. In panel a, $\theta_c = \theta'_s = 60°$ and $\phi'_s = 180°$, so that the wind is in the **x**-direction, i.e., blowing from the top to the bottom of the diagram. In panel b, $\theta_c = \theta'_s = 60°$ again, but now $\phi'_s = 90°$, so that the wind is blowing from left to right. The field of view of the water surface is directed along $-\mathbf{a}$ in Fig. 6, and the viewing angles ψ_h and ψ_v are displayed along with contours of the water facet azimuth and tilt angles α and β. An interesting point to observe in Fig. 8 is that the crosswind glitter pattern in panel b is slightly broader in the left–right direction and less elongated in the vertical direction than the alongwind pattern of panel a. This is expected on physical grounds since $\sigma_u^2 > \sigma_c^2$.

Figure 9 shows for comparison an air-incident, reflected glitter pattern photograph by Cox and Munk for the case of $\theta'_s = 60°$, $U = 4.6$ m s^{-1} and an unknown ϕ'_s. The major features of the random part of the photograph's pattern are well reproduced by the Monte Carlo simulation. By implementing the gravity wave procedures of appendix C in PM, the gravity waves in the photograph can also be simulated.

Figure 10 shows the development of an air-incident capillary-wave reflected glitter pattern as a function of wind speed (camera position A of Fig. 7). Other parameter values are the same as in Fig. 8, except that a wider angle view is taken. In panel a of Fig. 10, we see a small, very dense pattern for a wind speed of 1 m s^{-1}. As the wind increases through 5, 10 and 20 m s^{-1} in panels b, c and d, the glitter pattern becomes larger and less dense at its center. From the β contours of Fig. 10a, we see that at $U = 1$ m s^{-1} only rarely is a wave facet normal tilted by as much as 10° from the vertical, the bulk being less than 5°. At winds of 20 m s^{-1}, Fig. 10d shows occasional facet tilts of β greater than 30°.

Figure 11 illustrates the dependence of the air-incident reflected glitter pattern on solar position for a given wind speed of 5 m s^{-1}. Panel a of Fig. 11 shows a pattern for the light source at $\theta'_s = 1.0°$ and $\phi'_s = 180°$. The camera (as in A of Fig. 7) is essentially looking straight down with the sun overhead. The pattern is nearly circular, although there is a slight elongation in

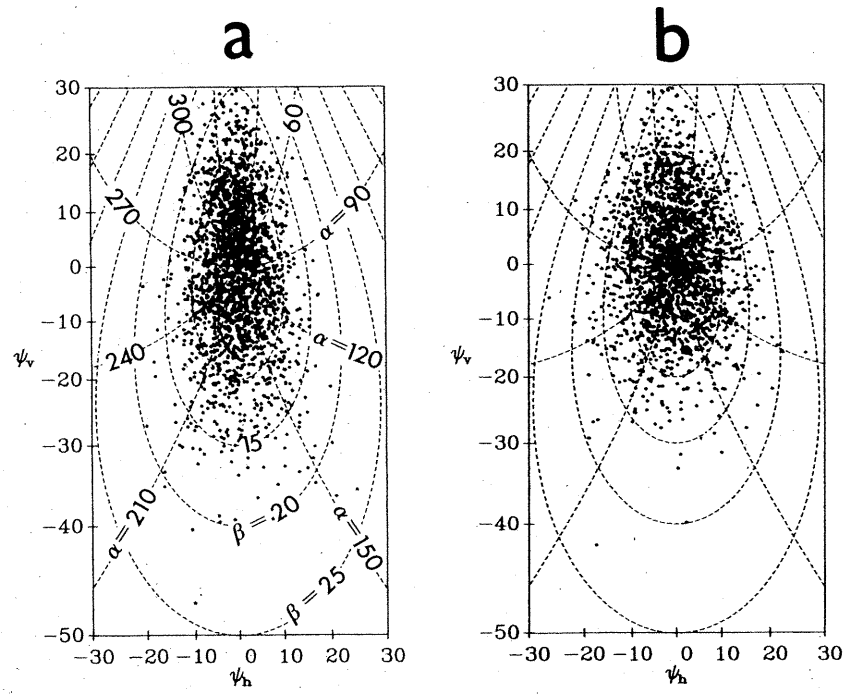

FIG. 8. Monte Carlo generated glitter patterns for comparison with Fig. 9. Panel (a) has parameter values $\theta'_s = 60°$, $\phi'_s = 180°$, $\theta_c = 60°$ and $U = 5$ m s^{-1} with 2000 points plotted. Panel (b) is the same except that $\phi'_s = 90°$. ϕ'_s is measured positive counterclockwise from i in the wind-based system.

the alongwind direction (top to bottom of the picture) due to the anisotropy of the capillary wave surface. Figure 11b has $\theta'_s = 80°$ and $\phi'_s = 180°$, and Fig. 11c has $\theta'_s = 80°$ and $\phi'_s = 90°$. Just as in Fig. 8, we see in panels b and c an elongation of the pattern for the alongwind source location compared to the pattern for the crosswind source location. The glitter patterns are now becoming elongated into the "road to happiness" (Shuleikin, 1968, p. 383) due to the nearly horizontal angle of incidence of the incoming rays. Figure 11d shows the case of a setting sun, $\theta'_s = 90°$ and $\phi'_s = 180°$. The "road to happiness" is now fully developed.

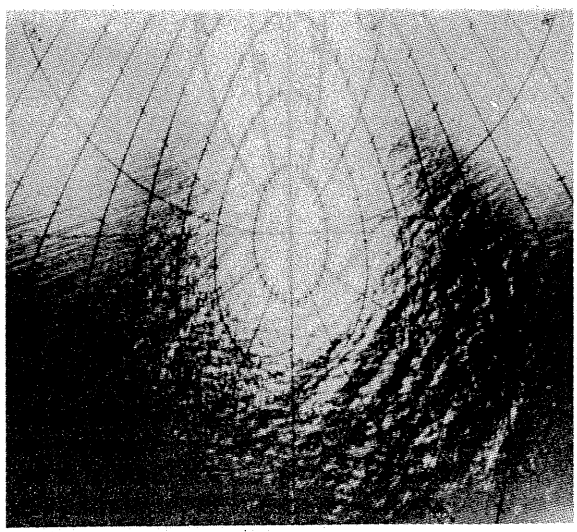

FIG. 9. Photograph of a glitter pattern on the open ocean. The conditions were similar to those modeled in Fig. 8.

The above Figs. 8–11 have all been for the usual case of air-incident reflected rays (camera position A in Fig. 7). Cox and Munk (1955) also estimated the appearance of glitter patterns of air-incident transmitted rays as seen from below the water surface (camera position B of Fig. 7). Figure 12a shows our glitter pattern for air-incident transmitted rays for the same parameter values as those of the reflected rays in Fig. 11a. The camera is looking essentially straight up toward the sun. The glitter pattern is much more compressed relative to Fig. 11a, as is expected from the laws of geometric optics. Only 500 points are plotted, due to the compactness of the pattern. Figure 12b shows the air-incident transmitted ray pattern for the same parameter values as Fig. 8a, namely $\theta'_s = 60°$, $\phi'_s = 180°$ and $U = 5$ m s^{-1}. The camera angle is now $\theta'_c = 40.5°$, as determined by the specular transmission direction. Most of the 2000 transmitted rays in Fig. 12b deviate less than 10° from the specular direction, as seen from the ψ_h and ψ_v values, although there is a noticeable sprinkling of points below and outside the main pattern. Figures 12c and 12d have $\theta'_s = 85°$, $\phi'_s = 180°$ and $\theta_c = 48.3°$. Figure 12c has $U = 5$ m s^{-1} and Fig. 12d has $U = 20$ m s^{-1}. In each of these figures the

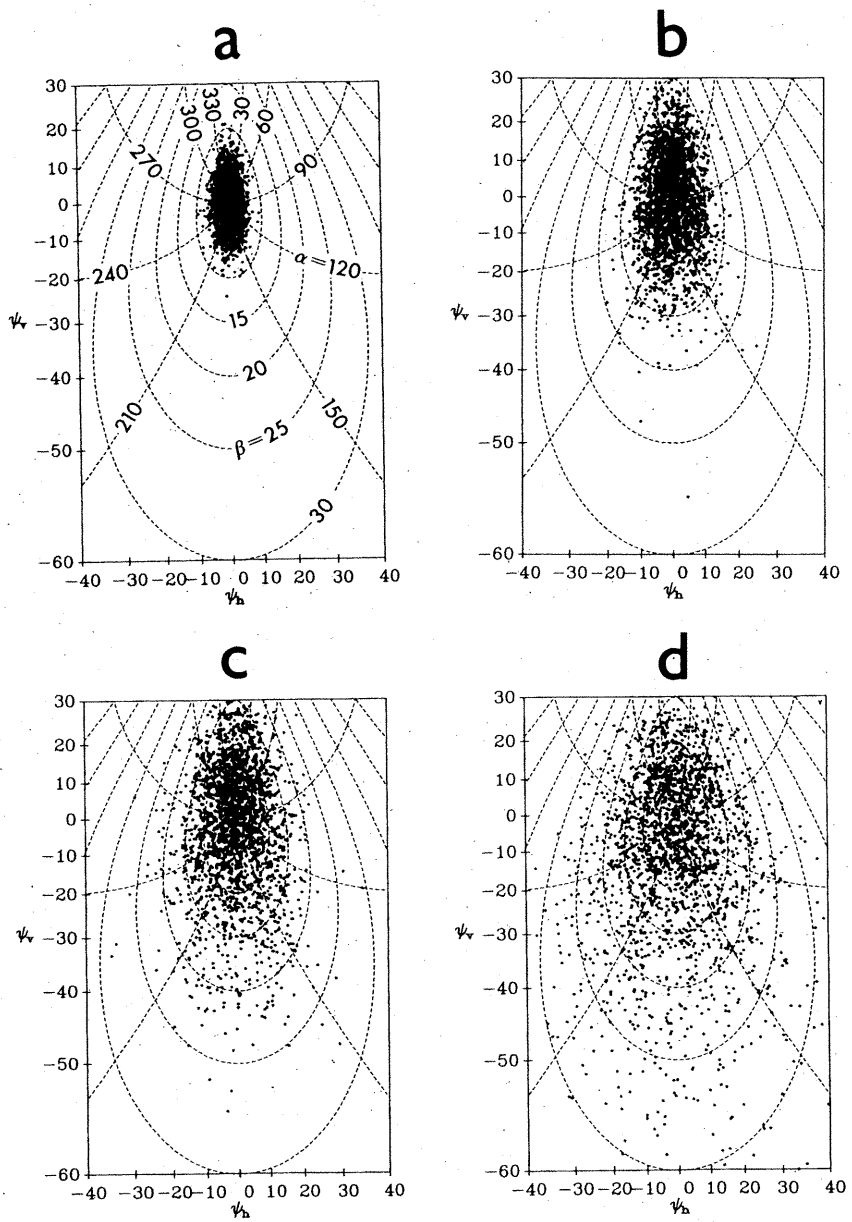

FIG. 10. Dependence of the reflected glitter pattern on wind speed for a fixed air-incident light source. Each diagram is for $\theta_s' = 60°$, $\phi_s' = 180°$, $\theta_c = 60°$ with 2000 points. Panel (a) is for $U = 1$ m s^{-2}, (b) 5 m s^{-1}, (c) 10 m s^{-1}, and (d) 20 m s^{-1}.

glitter pattern is shifted away from the specular transmission direction. As in the reflected ray case, an increasing wind speed gives a more diffuse pattern, although the effect is not as pronounced in the case of transmitted rays.

Glitter patterns for water-incident reflected rays (camera position C in Fig. 7), in the form of dot-density diagrams, appear on the whole the same as those for air-incident reflected rays (camera position A in Fig. 7), since the presently constructed random capillary surface appears on average the same from above or below. However, if the glitter patterns were generated with the dot size proportional to the radiant flux of the rays, then the patterns for water-incident reflected rays would appear brighter than those of the air-incident case, because of the greater Fresnel reflectance for water-incident rays.

The patterns for water-incident transmitted rays in principle should be much different from those of the air-incident transmitted case. In Fig. 13, panels a, b and c show various patterns for the case of $U = 5$ m s^{-1}. Figure 13a shows the pattern for rays passing almost straight up through the surface (camera position D in Fig. 7 with the camera looking almost straight down).

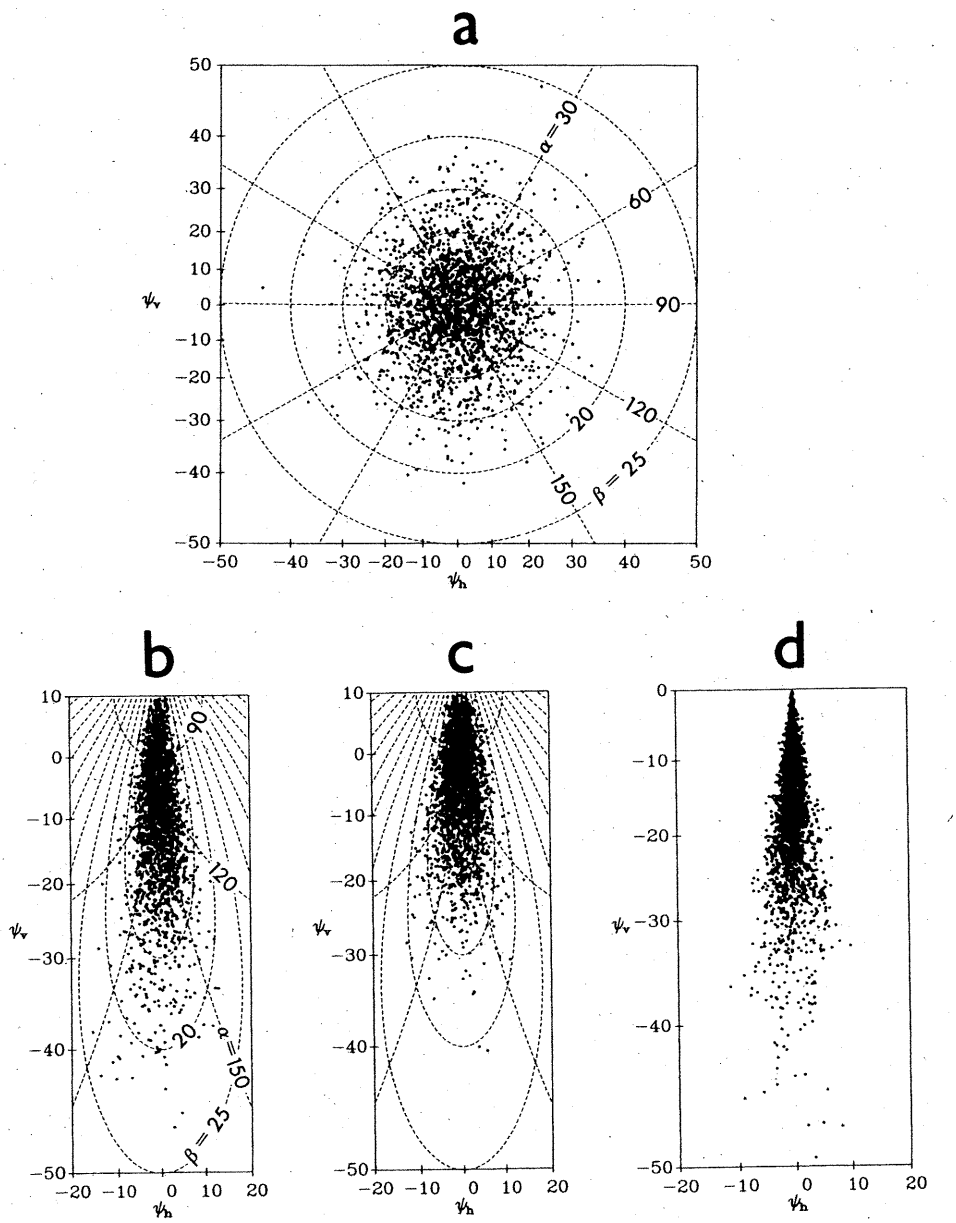

FIG. 11. Dependence of the reflected glitter pattern on light source location for air-incident rays. For each panel the wind speed is 5 m s^{-1}, $\theta_c = \theta'_s$, and 2000 points are plotted. Panel (a) has $\theta'_s = 1°$, $\phi'_s = 180°$, (b) $\theta'_s = 80°$, $\phi'_s = 180°$, (c) $\theta'_s = 80°$, $\phi'_s = 90°$, and (d) $\theta'_s = 90°$, $\phi'_s = 180°$.

The pattern is not as compact as the corresponding air-incident case of Fig. 12a and is in accord with the well-known magnification effect of the water surface on submerged objects. Figure 13b shows the case for a water-incident angle of $\theta'_s = 45°$ and $\phi'_s = 180°$ for a unidirectional source spatially distributed just below the water surface, with $\theta_c = 70.5°$. This θ'_s is measured from the nadir and is near the critical angle of 48.59° for total internal reflection in the specular case. For the wind speed of 5 m s^{-1} shown in Fig. 13b, only 1369 of 2000 incident rays were transmitted; the other 631 rays encountered facets which were tilted so as to cause total internal reflections. Figures 13c and 13d both have $\theta'_s = 60°$ and $\phi'_s = 180°$. For a specular surface there would be no transmitted rays at this value of θ'_s; therefore, the camera angle is set to $\theta_c = 90°$. Note from the ψ_v values that the tops of the figures are at the horizon and the entire view is then downward toward the water surface. As the wind increases from 0 to 5 m s^{-1}, and on to 20 m s^{-1}, an occasional facet is sufficiently tilted so as to transmit a ray through the surface. At $U = 5$ m s^{-1}, shown in Fig. 13c, 105 of 2000 incident rays passed through the surface to generate a sparse glitter pattern. At $U = 20$ m s^{-1}, shown in Fig. 13d,

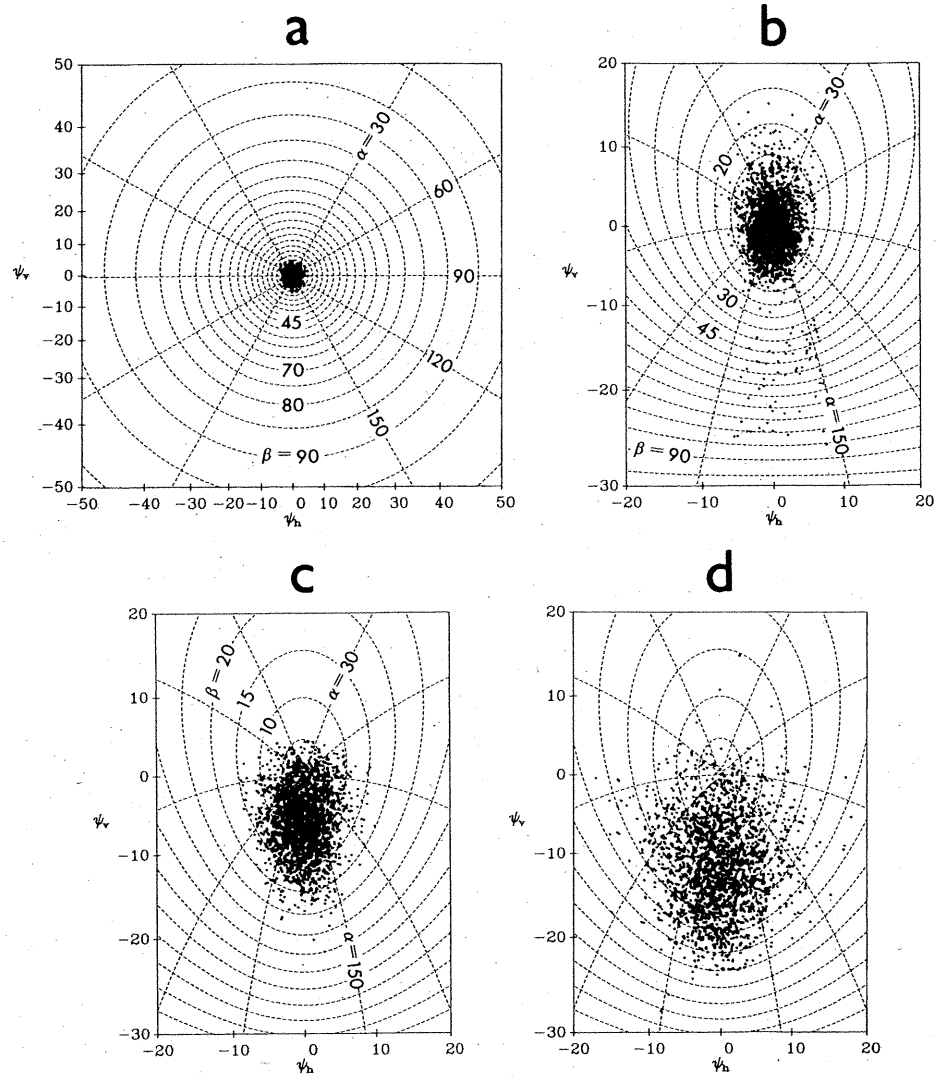

FIG. 12. Glitter patterns for air-incident transmitted rays. Panel (a): $\theta'_s = 1°$, $\phi'_s = 180°$, $\theta_c = 0.7°$, $U = 5$ m s^{-1} and 500 points plotted. Panel (b): $\theta'_s = 60°$, $\phi'_s = 180°$, $\theta_c = 40.5°$, $U = 5$ m s^{-1} and 2000 points. Panels (c) and (d): $\theta'_s = 85°$, $\phi'_s = 180°$, $\theta_c = 48.3°$ and 2000 points for (c) $U = 5$ m s^{-1} and (d) $U = 20$ m s^{-1}.

468 of 2000 rays were able to pass through the surface. Note that some glitter points lie beyond the $\beta = 90°$ contour. The rays which generated these points are the end products of multiple-scattering events, for which an equivalent single-scattering event would require an overturned water facet.

8. First-order ray scatter theory

The glitter patterns presented in the previous section were generated by rays which use the full power of the present ray-tracing model. In compiling the patterns no distinction was made between rays which intersected the image plane after a single scattering and those which were the final products of a multiple-scattering event. But it is of interest to know, for example, what contribution multiply scattered rays make to a glitter pattern. One approach to this problem would be to alter the ray-tracing code so that multiply scattered rays are ignored and the glitter pattern is generated by singly scattered rays only. The two glitter patterns could then be compared. Another approach is that of comparing an exactly produced Monte Carlo glitter pattern with one predicted by an analytic first-order theory; this approach is the topic of this section.

a. Outline of theory

On the assumption that the water surface is undulating gently, various nonlinear features of the surface and of the resulting glitter pattern theory can be neglected. The result is a simple linear theory which pre-

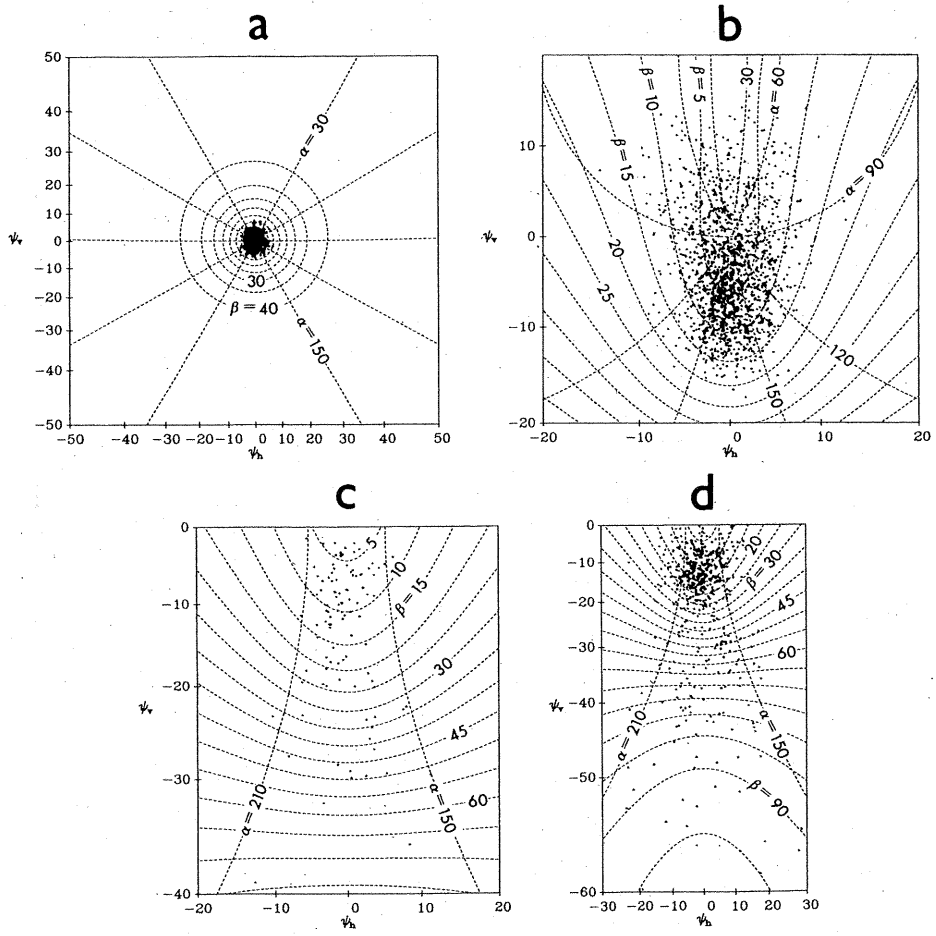

FIG. 13. Glitter patterns for water-incident transmitted rays. θ'_s is now measured from the nadir to the source location. Panel (a): $\theta'_s = 1°$, $\phi'_s = 180°$, $\theta_c = 1.3°$, $U = 5$ m s^{-1} and 500 points plotted. Panel (b): $\theta'_s = 45°$, $\phi'_s = 180°$, $\theta_c = 70.5°$, $U = 5$ m s^{-1} and 1369 points. Panels (c) and (d): $\theta'_s = 60°$, $\phi'_s = 180°$ and $\theta_c = 90°$ for (c) $U = 5$ m s^{-1} and 105 points and (d) $U = 20$ m s^{-1} and 468 points.

dicts the shape and dot-density distribution of a glitter pattern. We now develop a linearized theory for rays reflected by capillary waves. The theory is inspired by some notes of Eckart (1946).

Let ζ be a realization of a random function defined on the wind-based **i**–**j** plane of Fig. 6, the mean sea surface; ζ simulates the water surface and is assumed to be continuously differentiable. Let ζ_u and ζ_c be the slopes of the realized water surface in the upwind and crosswind directions, respectively. The joint probability density $p(\zeta_u, \zeta_c)$ of occurrence of these slopes is assumed to be a binormal distribution of the form (5) where σ_u^2 and σ_c^2 are given in (1). Observe that ζ_u and ζ_c are assumed to be independent random variables. The unit normal to the wave surface is given by

$$\mathbf{n} = (1 + \zeta_u^2 + \zeta_c^2)^{-1/2}(-\zeta_u\mathbf{i} - \zeta_c\mathbf{j} + \mathbf{k}). \qquad (7)$$

Thus **n** is measured in the wind-based coordinate system of Fig. 1 or Fig. 6, which we recall has the wind in the $+\mathbf{i}$ direction. If the surface is only slightly perturbed, the wave slopes ζ_u and ζ_c are small in magnitude, and the higher order terms ζ_u^2 and ζ_c^2 in (7) can be neglected. Thus an approximate first-order surface normal is

$$\mathbf{n} \approx -\zeta_u\mathbf{i} - \zeta_c\mathbf{j} + \mathbf{k}. \qquad (8)$$

We now have the option of choosing an air-incident or a water-incident ray ξ', and also the option of choosing a reflectance or a transmittance calculation. To fix ideas, we consider the following. An air-incident ray $\xi' \equiv \xi'_u\mathbf{i} + \xi'_c\mathbf{j} + \xi'_3\mathbf{k}$ is reflected into a direction ξ given by

$$\xi = \xi' - 2(\xi' \cdot \mathbf{n})\mathbf{n}.$$

This is the vector form of the law of reflection of a ray ξ' incident on a plane facet with normal **n**. Substituting the approximate normal **n** from (8) gives an approximate ξ, which in wind-based component form becomes

$$\xi \approx (\xi'_u, \xi'_c, -\xi'_3) + 2(\xi'_3\zeta_u, \xi'_3\zeta_c, \xi'_u\zeta_u + \xi'_c\zeta_c)$$

$$\equiv \xi_0 + \epsilon.$$

Here $\xi_0 \equiv (\xi'_u, \xi'_c, -\xi'_3)$ is the specular reflection direction for ξ' and

$$\epsilon \equiv 2(\xi'_3\zeta_u, \xi'_3\zeta_c, \xi'_u\zeta_u + \xi'_c\zeta_c)$$

is a *deflection vector* (in the wind-based system) representing the difference between the specular reflection direction ξ_0 and the actual (although approximate) reflection direction ξ. Note that ξ_0 and ϵ are perpendicular, i.e., that $\xi_0 \cdot \epsilon = 0$. Since ζ_u and ζ_c are independent normal variates distributed as in (5), the deflection vector ϵ is a random vector whose three components are normal random variates of zero means and variances $4\xi'^2_3\sigma_u^2$, $4\xi'^2_3\sigma_c^2$, and $4(\xi'^2_u\sigma_u^2 + \xi'^2_c\sigma_c^2)$, respectively, in the **i–j–k** coordinate system. [If we had chosen the air-incident transmittance option, then we would have used the ξ_t (Snell's law) representation with the form of **n** given by (8) and would have obtained a similar decomposition $\xi_0 + \epsilon$ of ξ.]

Since ξ_0 and ϵ are perpendicular, it is possible to define a *deflection plane* which is analogous to the image plane in Fig. 6. Accordingly, we are guided by the image plane concept of Fig. 6 and set $f = 1$, $\mathbf{a} = \xi_0$, and recall that $\mathbf{z} = \mathbf{k}$ in both sun and wind-based systems. Then define the deflection plane coordinate axis unit vectors **h** and **v** as $\mathbf{h} \equiv (\xi_0 \times \mathbf{k})/\|\xi_0 \times \mathbf{k}\|$ and $\mathbf{v} \equiv \xi_0 \times \mathbf{h}$. Substituting ξ_0 in these relations and rearranging we find

$$\mathbf{h} = (\xi'^2_u + \xi'^2_c)^{-1/2}(\xi'_c\mathbf{i} - \xi'_u\mathbf{j})$$

$$\mathbf{v} = -(\xi'^2_u + \xi'^2_c)^{-1/2}[(\xi'_u\xi'_3)\mathbf{i} + (\xi'_c\xi'_3)\mathbf{j} + (\xi'^2_u + \xi'^2_c)\mathbf{k}],$$

as measured in the wind-based system. We can measure ϵ in the deflection plane, relative to the basis **h**, **v** as

$$\epsilon_h \equiv \epsilon \cdot \mathbf{h} = 2\xi'_3(\xi'^2_u + \xi'^2_c)^{-1/2}(\xi'_c\zeta_u - \xi'_u\zeta_c)$$

$$\epsilon_v \equiv \epsilon \cdot \mathbf{v} = -2(\xi'^2_u + \xi'^2_c)^{-1/2}(\xi'_u\zeta_u + \xi'_c\zeta_c).$$

Noting that

$$\cos\phi' = \xi'_u(\xi'^2_u + \xi'^2_c)^{-1/2}$$

$$\sin\phi' = \xi'_c(\xi'^2_u + \xi'^2_c)^{-1/2},$$

where ϕ' is the azimuth angle of the ξ' vector measured positive counterclockwise from **i** in the **i–j** plane to the **x**-axis (cf. Fig. 6), we find

$$\epsilon_h = 2\xi'_3(\zeta_u \sin\phi' - \zeta_c \cos\phi')$$

$$\epsilon_v = -2(\zeta_u \cos\phi' + \zeta_c \sin\phi'). \tag{9}$$

Equation set (9) gives the desired first-order theory of the glitter pattern. The interpretation of (ϵ_h, ϵ_v) is that of a randomly located point in the deflection plane. Since ζ_u and ζ_c are normal random variables of zero mean, so too are ϵ_h and ϵ_v. The second order moments of ϵ_h and ϵ_v are

$$\left.\begin{aligned} E\{\epsilon_h^2\} &\equiv \sigma_h^2 = 4\xi'^2_3(\sigma_u^2 \sin^2\phi' + \sigma_c^2 \cos^2\phi') \\ E\{\epsilon_v^2\} &\equiv \sigma_v^2 = 4(\sigma_u^2 \cos^2\phi' + \sigma_c^2 \sin^2\phi') \\ E\{\epsilon_h\epsilon_v\} &= 4\xi'^2_3(\sigma_c^2 - \sigma_u^2)\cos\phi' \sin\phi' \end{aligned}\right\}, \tag{10}$$

where E is the ensemble average operator which averages the indicated quantity over all realizations of the random surface ζ. Therefore the (ϵ_h, ϵ_v) points in the deflection plane for the case $\phi' = 0°, 90°, 180°$ or $270°$ obey a normal probability density function in which ϵ_h and ϵ_v are uncorrelated:

$$p(\epsilon_h, \epsilon_v) = (2\pi\sigma_h\sigma_v)^{-1} \exp\left[-\frac{1}{2}\left(\frac{\epsilon_h^2}{\sigma_h^2} + \frac{\epsilon_v^2}{\sigma_v^2}\right)\right]. \tag{11}$$

Observe, from the presence of ξ'_3 in $E\{\epsilon_h^2\}$, how the predicted glitter pattern becomes elongated toward the horizon as the light source descends toward the horizon.

b. *A test of the theory*

Equation (11) suggests a means of comparing the set of ray dots of a Monte Carlo produced glitter pattern, or even an actual glitter pattern, with that of the first-order theory under identical conditions. If the compared patterns of ray dots are sufficiently close, then the first-order theory is deemed adequate; otherwise, the first-order theory fails, perhaps because higher-order processes (multiple scattering, or shielding, or nonlinear hydrodynamics) have in some way distorted the glitter pattern. In this manner we can determine the parameter values (e.g., wind speed and incident ray direction) for which a first-order theory is a reasonable approximation to reality. We shall compare the present first-order theory with the Monte Carlo procedure.

One matter remains before making this comparison of ray-dot patterns. The (ϵ_h, ϵ_v) points refer to the deflection plane of the first-order model, but the glitter pattern points (t_h, t_v) refer to the image plane of the Monte Carlo model. We must be able to convert (ϵ_h, ϵ_v) values into (t_h, t_v) values, and vice versa. The details of such transformations are given in PM. In Fig. 6, for such transformations we set $f = 1$ and $\mathbf{a} = \xi_0$, so that the image and deflection planes are well-defined and coincide.

Suppose now we partition the deflection plane into regions defined by concentric ellipses about the origin of the plane. Each ellipse has some "radius" ϵ, and the set of points (ϵ_h, ϵ_v) on this ellipse obey the equation

$$\frac{\epsilon_h^2}{\sigma_h^2} + \frac{\epsilon_v^2}{\sigma_v^2} = \epsilon^2, \tag{12}$$

where σ_h^2 and σ_v^2 are given in (10) for the case of $\phi' = 0$. Now using (11) it may be shown (see PM) that the probability $Q(\epsilon)$, $0 \leq Q(\epsilon) < 1$, of a randomly chosen point (ϵ_h, ϵ_v) in the deflection plane falling within the elliptical region defined by the ellipse of radius ϵ, is given by

$$Q(\epsilon) = 1 - \exp\left[-\frac{1}{2}\epsilon^2\right], \quad 0 \leq \epsilon < \infty. \tag{13}$$

Conversely, we have from this the relation

$$\epsilon = [-2\log(1 - Q)]^{1/2} \tag{14}$$

that defines the radius of a deflection plane ellipse whose interior region contains an amount Q of probability mass.

Next, selecting values of $Q = 0.5$, 0.9 and 0.99, say, Eqs. (12) and (14) allow us to draw the (ϵ_h, ϵ_v)-ellipses in the deflection plane which contain 50, 90 and 99 percent of the randomly distributed (ϵ_h, ϵ_v) points, respectively. Then the points of the Monte Carlo produced glitter pattern are mapped onto the deflection plane via the (t_h, t_v) to (ϵ_h, ϵ_v) mapping alluded to above. The numbers of actual ray points in the Monte Carlo produced glitter pattern which fall within the various elliptical contours of Q are then counted. A χ^2 goodness-of-fit test between the numbers of points predicted by first-order theory and the observed numbers of ray points in the mapped glitter pattern is then made. The hypothesis being tested is

H_0: The glitter pattern (distribution of points in the image plane) produced by Monte Carlo ray tracing is compatible with the first-order theory.

The χ^2 test is performed as follows. The values $Q = 0.5$, 0.9 and 0.99 define four disjoint classes of points that partition the deflection plane into an elliptical region, two elliptical annuli and one infinite region whose probability masses under the null hypothesis H_0 are respectively $p_1 = 0.5$, $p_2 = 0.4$, $p_3 = 0.09$ and $p_4 = 0.01$. In a deflection plane glitter pattern of N points mapped from the image plane, let N_j be the number of mapped points falling in the jth of the four deflection plane probability classes (thus $N_1 + N_2 + N_3 + N_4 = N$). Then set

$$\chi^2 = \sum_{j=1}^{k=4} \frac{(N_j - Np_j)^2}{Np_j} . \qquad (15)$$

We choose to test H_0 at the $\alpha = 0.01$ significance level, for which the critical value is $\chi^2(\alpha, k-1) = \chi^2(0.01, 3) = 11.325$. We then accept or reject H_0 according to the following scheme:

$$\left.\begin{array}{ll} \text{accept } H_0 & \text{if } \chi^2 < \chi^2(\alpha, k-1) \\ \text{reject } H_0 & \text{if } \chi^2 \geq \chi^2(\alpha, k-1) \end{array}\right\} .$$

Figure 14 shows three glitter patterns in the image plane produced by the Monte Carlo ray-tracing procedure. The parameters in each pattern differ only in the incident θ'_s values used. For each panel, $\phi'_s = 180°$, $U = 5$ m s^{-1} and $N = 2000$ points are plotted. The Q-labeled contours in the image plane are the transformations, under the (ϵ_h, ϵ_v) to (t_h, t_v) mapping, of the elliptical contours in the deflection plane which enclose probability masses of $Q = 0.5$, 0.9 and 0.99 according to the first-order theory. From the image plane vantage point it is not easy for the eye to discern from Fig. 14 whether or not each pattern should lead to an acceptance of H_0. The transformed and somewhat distorted ellipses in panels b and c should give a preliminary

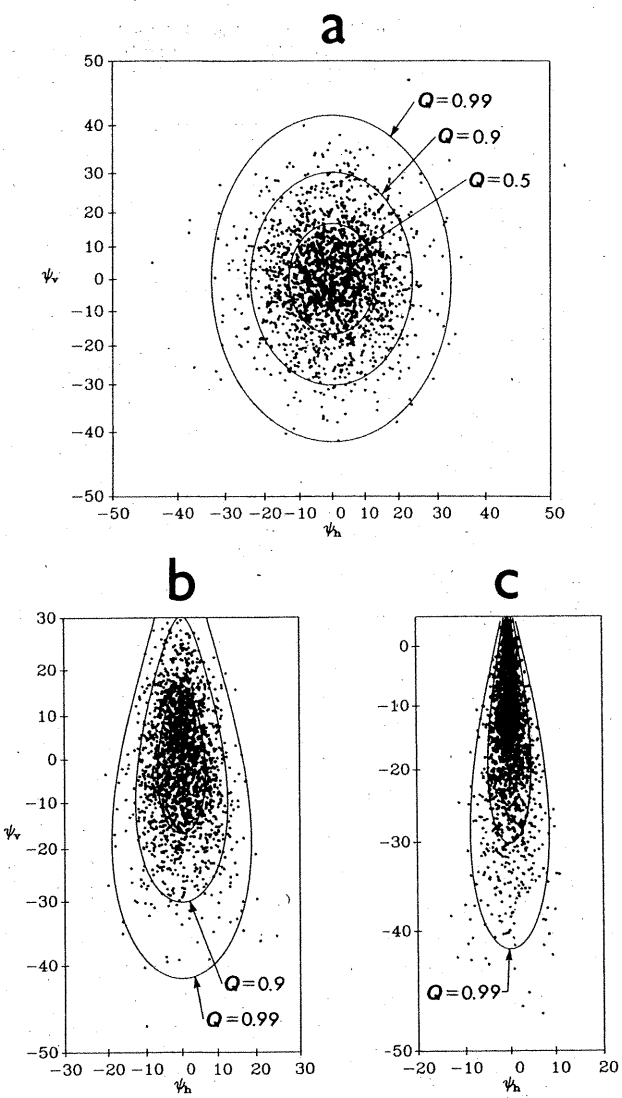

FIG. 14. Testing the first-order theory. Glitter patterns in the image plane for air-incident reflected rays. The transformed (mapped) ellipses are those defined by first-order theory and define elliptical regions containing probability masses $Q = 0.5$, 0.9 and 0.99. These ellipses are mapped into the image plane of the Monte Carlo method using the (ϵ_h, ϵ_v) to (t_h, t_v) mapping. Each panel has $\phi'_s = 180°$, $\theta_c = \theta'_s$, $U = 5$ m s^{-1} and 2000 points. Panels (a) $\theta'_s = 1°$, (b) $\theta'_s = 60°$ and (c) $\theta'_s = 85°$.

indication that the first-order theory is perhaps not adequate in all these cases. However, the above-defined χ^2 counting test in the deflection plane is easily made.

The results of testing H_0 for the three patterns of Fig. 14 are displayed in Table 1. Here we see that for the $\theta'_s = 1°$ case of Fig. 14a, the Monte Carlo realized distribution of points is close to that predicted by first-order theory, leading to a very small χ^2 of 0.720 and thus acceptance of H_0. The case of $\theta'_s = 60°$ has a Monte Carlo produced pattern with χ^2 less than the critical value, so H_0 is accepted. However, for the $\theta'_s = 85°$ case of Fig. 14c, the glitter pattern, according to

TABLE 1. Example results of χ^2 tests for the glitter patterns of Fig. 14. The displayed results are for $U = 5$ m s^{-1} and 2000 rays coming from a source at $\phi'_s = 180°$, with the indicated θ'_s values.

Populations	θ'_s (deg)	Categories $0 \leq Q \leq 0.5$	$0.5 < Q \leq 0.9$	$0.9 < Q \leq 0.99$	$0.99 < Q \leq 1$	χ^2	Comments
Category populations expected under hypothesis H_0	—	1000	800	180	20	11.325	Critical value $\chi^2(\alpha, k-1) = \chi^2(0.01, 3)$
Realized category populations	1	985	806	189	20	0.720	Clear acceptance
	60	1044	796	147	13	10.456	Borderline acceptance
	85	837	862	261	40	87.824	Clear rejection

the contours, is relatively diffuse; i.e., not enough points fall in the central part of the pattern and too many fall in the outer regions, causing χ^2 to be large and thus H_0 to be rejected. Hence in this case the first-order theory is not adequate to describe the Monte Carlo produced results.

The results of testing H_0 systematically for a variety of 2000-point glitter patterns are summarized in Fig. 15. In this figure cases of clear acceptance or rejection of the χ^2-test hypothesis H_0 at the $\alpha = 0.01$ level are indicated by "A" or "R" respectively. Borderline cases where $\chi^2 \approx \chi^2(\alpha, k-1)$, as was the case of Fig. 14b, are indicated by "B." This figure gives a rough idea of where the first-order theory is adequate. More extensive testing would have to be done in order to accurately fix the boundary line and in order to determine the weak dependence on ϕ'_s (all points in Fig. 15 are for $\phi'_s = 180°$, with some points recomputed for $\phi'_s = 90°$). We note from Fig. 15 that the first-order theory holds over a great range of θ'_s values for very low wind speeds, as expected, since the surface is then quite smooth and locally nearly level. However, for incident angles near $\theta'_s = 0$ (rays coming nearly straight down), the first order theory also holds for high wind speeds. This probably reflects the fact that only single-order scattering occurs for rays coming from near the zenith, even though the rms slopes at $U = 20$ m s^{-1} are of order $\zeta_u \sim 0.25$ so that $\zeta_u^2 \sim 0.06$. For nearly horizontal incident rays, the first-order theory fails even at wind speeds of less than 1 m s^{-1}, for which the rms slopes are $\zeta_u \sim 0.05$ and $\zeta_u^2 \sim 0.003$. Presumably this failure of the first-order theory is due to the effects of multiple scattering and shielding, which become important at low incident angles, even at low wind speeds.

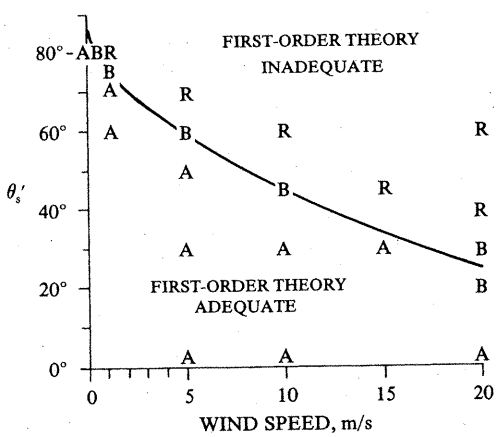

FIG. 15. The region of validity of first-order air-incident reflected glitter pattern theory, according to χ^2 testing at the $\alpha = 0.01$ significance level. An "A" ("R") indicates clear acceptance (rejection) of H_0, and a "B" indicates borderline acceptance or rejection at the $\alpha = 0.01$ level. Generally, for a given θ'_s, the first-order theory is acceptable for winds from zero up to some critical speed, beyond which it is not acceptable, as indicated.

c. *Application of the theory*

The first-order theory can be used to generate both glitter patterns and surface albedos of a wind-roughened sea surface. The calculations are relatively simple compared to those of the Monte Carlo ray-tracing procedure.

Under conditions on ξ' and U for which the first-order theory holds, one can simulate glitter patterns as follows. Suppose ξ' and U are given. Then σ_u^2 and σ_c^2 are determined and are related to U by means of Eq. (1). Next, generate n ($\sim$2000) pairs (ζ_u, ζ_c) of normal random variables by making n random independent selections from $N(0, \sigma_u^2)$ and $N(0, \sigma_c^2)$. For each of the n pairs (ζ_u, ζ_c) with ϕ' known from ξ', compute the associated deflection plane pair (ϵ_h, ϵ_v) using (9). A good simulation of a reflected glitter pattern for the air-incident case, for example, is obtained if one plots at the point (ϵ_h, ϵ_v) in the deflection plane a dot whose radius is proportional to the Fresnel reflectance defined by ξ' and $\mathbf{n}$, namely $r_-(\xi' \cdot \mathbf{n})$, where $\mathbf{n}$ is the wave facet normal given by (8). Note that the use of (9) imparts the correct "tilt" to the elliptical glitter pattern's major axis relative to the $\mathbf{h}$-axis in the deflection plane, so as to account for the relative azimuths of the wind and sun angles.

When the first-order theory holds, the surface albedos $r_\pm$ for arbitrary lighting conditions can be estimated in the following way. We begin as in the preceding glitter pattern simulation and generate $r_-(\xi' \cdot \mathbf{n})$, as described above, for each of the 2000 pairs (ζ_u, ζ_c). These reflec-

tances $r_-(\xi' \cdot \mathbf{n})$ are the first-order method's counterparts to $r_-(\xi';\omega)$ in (6), $\omega = 1, \cdots, 2000$. On averaging $r(\xi';\omega)$ over all ω, we obtain the corresponding value $r_-(\xi')$. This, in turn, is used in (17) below in the form $r_-(\theta'_s, \phi'_s)$, where (θ'_s, ϕ'_s) are the location angles for the source giving rise to ray ξ'.

In conclusion, we observe that, for each ξ', we can make four first-order glitter patterns or surface albedo quartet $(r_\pm, t_\pm)$ using the Fresnel reflectances or transmittances, $r_\pm(\xi' \cdot \mathbf{n})$ or $t_\pm(\xi' \cdot \mathbf{n})$, by adopting the four options outlined below (8). In this discussion we have illustrated the air-reflectance case. The theory of the three additional cases follows by suitably adapting the derivation outlined above.

9. Irradiance reflectances

We now turn our attention to the primary goal of this study: the computation of the irradiance reflectance, or albedo, of the sea surface as a function of wind speed, light source distribution, and scattering order.

Before describing the results we remark on the performance of the Monte Carlo method. As is generally known, sampling variability in Monte Carlo experiments is a source of numerical uncertainty in the desired results. Initial experiments with the ray-tracing model revealed that albedos $r_\pm(\xi')$ computed from ensemble averages based on 3000 surface realizations (with one ray ξ' per realization) are reproducible to within few percent of the desired magnitude for independent runs of 3000 realizations. We find that other possible sources of numerical error are completely negligible.

It should be noted that our reflectance results are those produced by infinitely distant single-direction light sources. The sun, while essentially infinitely distant, subtends a small but finite solid angle in the sky. There is, therefore, the possibility of error owing to the slight variation of the Fresnel reflectance for rays incident from different directions within the solar disk. A series of runs was made in which the incident rays ξ' were randomly distributed within a solid angle equal to the sun's and centered at the sun-center direction ξ'_0. These finite-disk $r_-(\xi')$ results were compared with the point-disk $r_-(\xi'_0)$ results. It was found that even for nearly horizontal angles of incidence, where the Fresnel reflectance varies the most, the difference between $r_-(\xi')$ and $r_-(\xi'_0)$ was generally less than one percent. At wind speeds of 20 m s^{-1}, the difference was at most a few percent. Thus, there seems to be no need to consider the sun to be anything more than a point light source, unless extremely accurate results are required.

We are therefore confident that the albedos presented below are accurate to within 5 percent for the assumed numerical model. The magnitude of errors due to auxiliary physical processes not modeled, in particular the presence of whitecaps at higher wind speeds, and for polarized incident flux is not known. It is, however, likely that our results for unpolarized incident flux are accurate to within a few percent at low wind speeds but may differ somewhat more from reality at very high wind speeds.

We now discuss the computed albedos $r_-(\xi')$ [cf. Eq. (6)] for a water surface covered by capillary waves. Figure 16 shows $r_-(\xi')$ $[=r_-(\theta'_s, \phi'_s)]$ as a function of wind speed for selected θ'_s and ϕ'_s values. By symmetry, we find $r_-(\theta'_s, \phi'_s) = r_-(\theta'_s, 180° - \phi'_s)$, and $r_-(\theta'_s, \phi'_s) = r_-(\theta'_s, -\phi'_s)$, for each θ'_s and $0° \leq \phi'_s \leq 360°$. Hence it is sufficient to determine $r_-(\theta'_s, \phi'_s)$ over the range $0° \leq \phi'_s \leq 90°$ for each θ'_s. Four curves are shown for each θ'_s value in Fig. 16. The solid lines are for the alongwind case, $\phi'_s = 0°$, in which the incoming rays are in the vertical plane parallel to the wind. The dashed lines are for the crosswind case, $\phi'_s = 90°$, in which the incoming rays are in the vertical plane perpendicular to the wind. In the computations a separate tally was kept for singly scattered rays so that the effects of multiple scattering could be isolated. For each pair of solid or dashed curves, the top curve gives the total albedo computed from all rays and the bottom curve gives the albedo as computed from singly scattered rays only. Most points on the curves of Fig. 16, above each labeled wind speed, are the average of three separate experiments (with 3000 surface realizations per experiment). Spot checks of the accuracy of these curves show that they are within a few percent of the true values (as

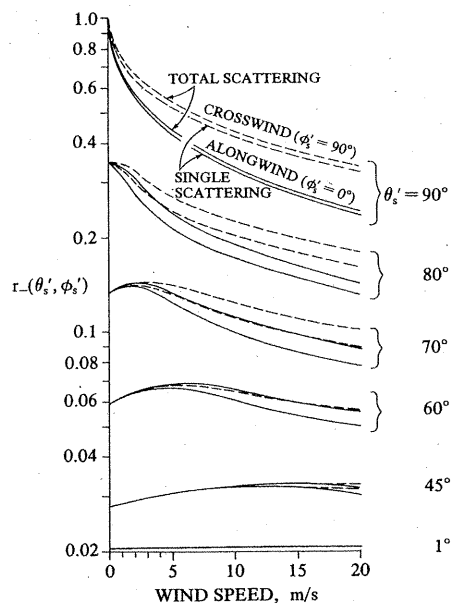

FIG. 16. Albedos (irradiance reflectances) $r_-(\theta'_s, \phi'_s)$ for random capillary waves, and parallel air-incident light rays (e.g., from distant point sources). For each group of θ'_s curves, the solid lines are for $\phi'_s = 0°$ (light rays and wind along same direction) and the dashed curves are for $\phi'_s = 90°$ (light source at right angles to wind direction). For each pair of solid or dashed curves, the top curve is for total scattering and the bottom curve is for single scattering only.

defined by an infinite number of surface realizations). For example, for the alongwind total scattering case of $U = 20$ m s^{-1} with $\theta'_s = 60°$, five experiments (of 3000 realizations each) yielded an average $r_-(\xi')$ value of 0.05456, with a standard deviation of 0.00053. For the same situation except for $\theta'_s = 80°$, the five experiment average yielded $r_-(\xi') = 0.14045$ with a standard deviation of 0.00128. Two of these standard deviations on each side of the curves will define points that are only slightly more separated than the drawn thickness of the curves. According to standard statistical reasoning, we are 95 percent confident that the true mean values lie between these points.

The albedos for zero wind speed in Fig. 16 are, of course, just the Fresnel reflectance of a horizontal plane surface (index of refraction $m = 4/3$) for the given θ'_s. For high solar altitudes (i.e., small θ'_s), the albedo increases slightly as the wind increases from zero, whereas for low solar altitudes, the albedo decreases markedly as the wind picks up. Therefore, in polar regions of the earth, low-sun power input to the ocean increases with wind speed. This qualitative behavior was predicted by Cox and Munk (1955) from approximate analytic calculations. The present study reveals in detail the quantitative features of this behavior, in particular the effects of wave anisotropy and multiple scattering.

A detailed view of the dependence of $r_-(\theta'_s, \phi'_s)$ on the azimuth angle ϕ'_s of the source relative to the wind direction is shown in Fig. 17. This figure gives the total-scattering albedo at a wind speed of 20 m s^{-1} for capillary waves. Since the wave facets are slightly less tilted, on average, in the crosswind direction than in the alongwind direction [recall that $\sigma_u^2 > \sigma_c^2$ in (1)], rays incident at right angles to the wind ($\phi'_s = 90°$) see a slightly flatter water surface and thus have a slightly higher albedo. This behavior is seen in Fig. 17. The

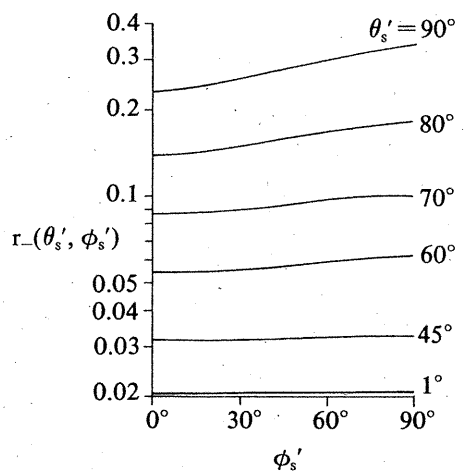

FIG. 17. Dependence of capillary-wave albedo $r_-(\theta'_s, \phi'_s)$ (including all scattered rays) on light source azimuth ϕ'_s relative to wind direction, for various zenith angles θ'_s and a wind speed of $U = 20$ m s^{-1}.

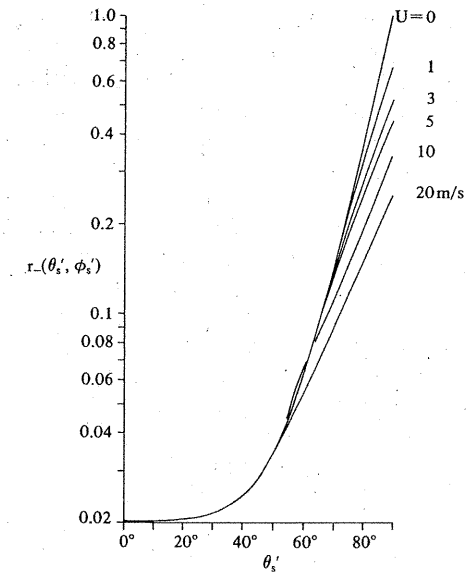

FIG. 18. Albedos as a function of wind speed and θ'_s, for $\phi'_s = 0°$ and a random capillary wave surface (replots of the upper solid curve of each solid pair in Fig. 16).

dependence is very weak at high sun altitudes (small θ'_s) but becomes substantial for incident angles near the horizon.

Figure 18 reproduces in different form the total scattering curves of Fig. 16 for the alongwind case, $\phi'_s = 0$. The form of Fig. 18 is more convenient if the albedo is desired for intermediate θ'_s values.

The albedos for an underwater light source, $r_+(\xi')$ [$=r_+(\theta'_s, \phi'_s)$], are shown in Fig. 19. Now θ'_s is measured from the nadir to the source location. The arrangement of the curves (alongwind, crosswind, total and single scattering) is analogous to that for the air-incident case in Fig. 16. However, the curves are strikingly different from their counterparts in Fig. 16 because of the effects of total internal reflection. For the specular surface at zero wind speed, any water-incident ray with $\theta'_s \geq \arcsin(1/m) = 48.59°$ (for $m = 4/3$), is totally reflected, giving an albedo of 1. The Fresnel reflectance increases quite rapidly as this limit is approached and, of course, is constant thereafter. As soon as the wind increases from $U = 0$, rays incident at $\theta'_s = 48.59°$ begin hitting tilted facets and sometimes experience only partial reflection; the albedo $r_+(\xi')$ then drops sharply for this θ'_s value. Rays water-incident at angles near the horizon are almost always totally reflected even at high wind speeds, so $r_+(\xi')$ remains extremely close to 1 at these angles. For angles of incidence $\theta'_s \leq 45°$ there is a strong dependence on θ'_s, unlike the air-incident case of Fig. 16. We see that increasing wind speed now causes a rapid increase in the albedos, with the alongwind values now generally (but not always) being greater than the crosswind values. Comparing the curves for total and single scattering shows that multiply scattered rays often make a substantial con-

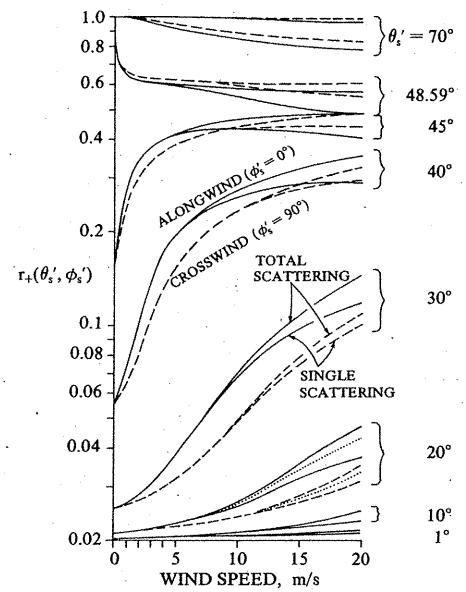

FIG. 19. Albedos (i.e., irradiance reflectances) $r_+(\theta_s', \phi_s')$ for random capillary waves and for parallel water-incident light rays. θ_s' is measured from the nadir to the source location. The solid and dashed line conventions are as in Fig. 16, and the dotted curve for $\theta_s' = 20°$ shows the grey convexification result for $\alpha = 0.5$ m^{-1}.

tribution to the albedo. The curves for total scattering assume that there is no attenuation of the radiant flux by the water for those ray paths which pass through the water from one facet to another. These curves thus correspond to a volume attenuation coefficient $\alpha = 0$; see the remarks below Eq. (6). The curves for single scattering are in essence the case of $\alpha = \infty$ (also known as black convexification[1]), since almost all possibilities for multiple scattering of water-incident rays are then eliminated. A case of "cloudy water" with $\alpha = 0.5$ m^{-1} is shown by the dotted lines in the $\theta_s' = 20°$ curves. (Since α is in units of meters^{-1}, $\delta = 1$ in (4) has units of meters for interpreting the dotted lines.) This serves to show that in practical calculations such as the present one, the optical properties of a random surface cannot be fully separated from those of the medium it bounds.[2]

Figure 20 replots selected total scattering curves (solid) from Fig. 19 in order to better show the dependence of $r_+(\xi')$ on θ_s'. A curve (dotted) with $\alpha = 0.5$ m^{-1} and the single-scattering curve (dashed) are also shown for a wind speed of 20 m s^{-1}. The steep slopes of these curves for the 20 m s^{-1} case show the importance of including multiple scattering in the r_+ estimates. The remaining solid curves are for total scattering, alongwind cases for the $U = 3$ m s^{-1} and $U = 0$ wind speeds shown.

The point source albedo $r_-(\xi')$ is a reasonable approximation to nature for the case of the sun in a clear sky. Likewise, $r_+(\xi')$ applies to a unidirectional light source just under the surface. However, in the air-incident case, if the sky is overcast the position of the sun may be indiscernible, so that an angularly extensive diffuse light source must be used in the calculations. Depending upon the exact form of the continuous radiance distribution over the appropriate hemisphere of incident directions, the albedo for a diffuse source is, in essence, a weighted average of the point-source albedos presented above. Albedos for angularly diffuse light sources can be computed with the Monte Carlo ray-tracing model by simply allowing the incoming ray directions to be distributed over the unit hemisphere according to the desired radiance distribution. For example, an albedo for a uniform sky could have ξ' values chosen at random such that each point in the dome of the sky is equally likely to be the source direction of the ray. We can expect that at least several tens of thousands of rays would need to be traced in order to get accurate albedos for diffuse sources. Rather than expending the considerable computational effort required for computing diffuse source albedos by direct ray tracing, we now describe a method which makes use of the point source albedos already computed.

A convenient parameterization for diffuse sky lighting in nature is the *cardioidal radiance distribution* (cf *H.O.*, Vol. VI, p. 21):

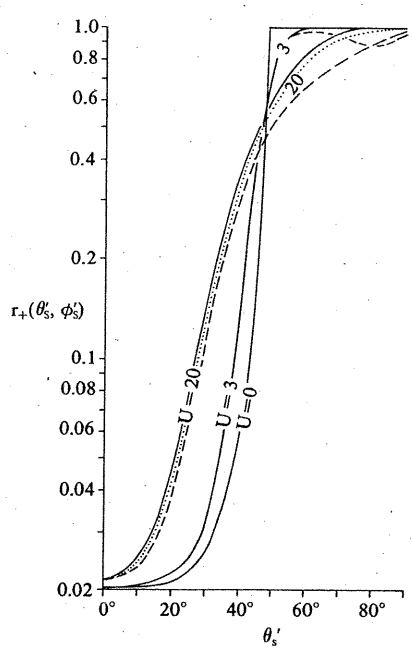

FIG. 20. Selected albedos $r_+(\theta_s', \phi_s')$ replotted from Fig. 17. The solid curves are for the alongwind total scattering cases for the wind speeds shown.

[1] Various convexification concepts are used in Preisendorfer (1965, pp. 77, 100) to formulate the application of invariant imbedding ideas to disconnected and concave optical media. Here, these concepts can be used to help organize the single and multiple scattering results.

[2] The analytic approach to random air–water surface reflectance calculations, as described in *H.O.* Vol. VI, §12.0–12.14, handles this separation problem in a satisfactory way. However, no numerical tests of that analytic approach have been made.

$$N(\theta', \phi') \equiv N_0(1 + c\cos\theta') \qquad (16)$$

where N_0 is the radiance of the horizon ($\theta' = 90°$), and c is a real parameter. For the case of a heavy overcast, observations indicate that $c = 2$, which summarizes the fact that on such a day the sky at the zenith ($\theta' = 0$) is three times as bright as the sky at the horizon. A sky over which N is uniform is given by $c = 0$. For water-incident rays, values of c in the range $-0.9 \leqslant c \leqslant -0.8$ are representative of the range of upwelling radiance distributions observed in natural waters, where θ' in (16) is now measured from the nadir. Thus a submerged skin diver looking toward his horizon may see five to ten times the brightness (radiance) that he sees looking straight down into the depths. That the subsurface horizon is much brighter than the nadir is a consequence, among other things, of the total internal reflection of rays which are incident on the bottom side of the water surface from nearly horizontal directions. Another reason may be based on the large ratio of forward to backward scattering values of the volume scattering function of lakes and seas (*H.O.*, Vol. I, pp. 125–132).

The albedo (irradiance reflectance) for a continuous radiance distribution is (*H.O.*, Vol. VI, p. 17)

$$r_{\pm} = \frac{\int_0^{2\pi}\left[\int_0^{\pi/2} N(\theta', \phi')r_{\pm}(\theta', \phi')\cos\theta'\sin\theta' d\theta'\right]d\phi'}{\int_0^{2\pi}\left[\int_0^{\pi/2} N(\theta', \phi')\cos\theta'\sin\theta' d\theta'\right]d\phi'}.$$

Here $r_{\pm}(\theta', \phi')$ is the Monte Carlo (or first-order analytic) point source albedo, and $r_{\pm}$ is the corresponding albedo for a continuous radiance distribution over the appropriate hemisphere. Substituting (16) for $N(\theta', \phi')$ and integrating gives

$$r_{\pm} = \frac{12}{(2c + 3)\pi}\int_0^{\pi/2}\left[\int_0^{1}(1 + c\mu')\mu' r_{\pm}(\mu', \phi')d\mu'\right]d\phi' \qquad (17)$$

after letting $\mu' \equiv \cos\theta'$. The integral (17) can be numerically evaluated using the point source albedos $r_{\pm}(\theta', \phi') \equiv r_{\pm}(\mu', \phi')$ already computed in drawing Figs. 16–20 (or already computed using the first-order analytic theory). The $r_{\pm}(\mu', \phi')$ values, known on a discrete (μ', ϕ') grid, are first fitted with a bicubic spline to generate a continuous representation of $r_{\pm}(\mu', \phi')$. This bicubic spline function is then substituted in (17) and the integration is numerically performed.

Figure 21 shows the albedo (irradiance reflectance) r_- for uniform sky and heavy overcast conditions as generated from the Monte Carlo procedure. The results for total (solid curve) and single scattering (dashed curve) were computed by using the corresponding values of $r_-(\xi')$ [$=r_-(\mu', \phi')$] in (17). For the case of no wind, $r_-(\xi')$ is the Fresnel reflectance function and (17) can be integrated analytically (cf. *H.O.*, Vol. VI, p. 26) to give $r_-(c = 0) = 0.0665$ and $r_-(c = 2) = 0.0513$ for the index of refraction $m = 4/3$. The values computed by the bicubic spline integrations are respectively $r_-(c = 0) = 0.0669$ and $r_-(c = 2) = 0.0519$ at $U = 0$. These comparisons indicate that the bicubic spline integration of (17) using the available point source albedos does not introduce any significant errors into the r_- values. We see that in general the albedos decrease with increasing wind speed and that the contribution by multiply scattered rays is significant at 5 m s^{-1} and above.

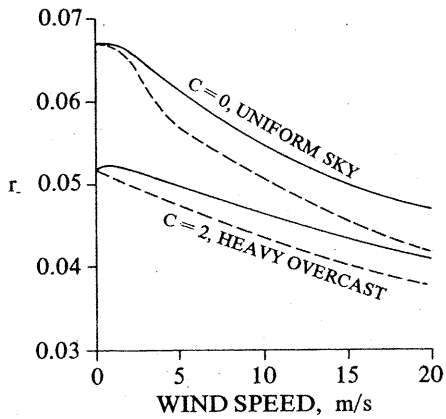

FIG. 21. Albedos r_- for continuous radiance distributions over the sky hemisphere. Solid lines are for total scattering and dashed lines are for single scattering only.

The diffuse light albedos for water-incident rays are shown in Fig. 22 for a variety of upwelling subsurface radiance distributions. Solid curves are for total scattering (with $\alpha = 0$), dashed curves are for single scattering, and dotted curves are for total scattering but with $\alpha = 0.5$ m^{-1}. For $U = 0$ and a uniform distribution ($c = 0$), Judd (*H.O.*, Vol. VI, p. 19) numerically estimated the value $r_+(c = 0) = 0.472$ for $m = 4/3$. Our integration of (17) for $U = 0$ yields $r_+(c = 0) = 0.486$, a difference of about 3 percent. We see that both for uniform ($c = 0$) and natural lighting conditions ($c = -0.7, -0.8, -0.9$), the total r_+ is only weakly dependent on wind speed in the total scattering case but is about an order of magnitude greater than r_-. The observed dip in r_+ at low wind speeds reflects the net effects of the relative importance for different θ'_s of the rapidly changing low wind speed values of $r_+(\theta'_s, \phi'_s)$ seen in Fig. 19. For the single scattering case, there is a significant decrease of r_+ with wind speed. Hence, in the final analysis, the inclusion of multiple scattering in the r_+ computations for a random air–water surface is of importance when relatively exact estimates are needed.

10. Comparison with observation

A few sets of observed sea surface albedos are available, and it is of interest to compare our computed results with these measured values. Payne (1972) determined albedos by measuring from a fixed platform

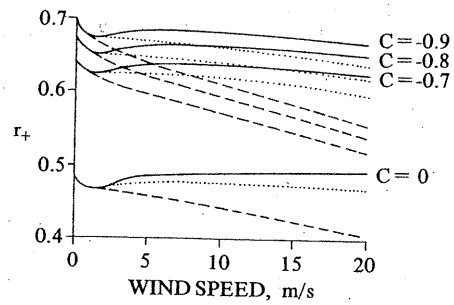

FIG. 22. Albedos r_+ for continuous radiance distributions over the sea hemisphere. Solid lines are for total scattering and white convexification (see text); dotted lines are for total scattering and grey convexification with $\alpha = 0.5\ m^{-1}$; dashed lines are for single scattering only, the equivalent of black convexification.

in coastal water the downward and upward irradiances above the sea surface. Simpson and Paulson (1979) repeated these measurements from a stable platform in mid-ocean. In these measurements, the upward irradiance is the sum of the downward irradiance reflected by the surface and the upward irradiance transmitted through the water surface from the ambient light field within the water. The observed albedo (the measured ratio of upward to downward irradiance just above the water surface) therefore depends on the optical properties of both the sea surface and the body of water below, besides the sky lighting conditions. Our albedo r_- depends only on the incident sky radiance distribution and on the random properties of the surface itself and thus corresponds to the reflected part only of the observed values. However, if the upward transmitted irradiance from the water body is small compared to the reflected irradiance from the sky, then our r_- should be nearly equal to, but less than, the measured values. Payne estimates that the upward transmitted irradiance contributes at most 15 percent of the measured upward irradiance. As a rule of thumb, relatively clear ocean and lake waters have a body albedo on the order of 0.02 over the visible spectrum (400–700 nm). Coastal waters with much biologic activity can have body albedos on the order of 10 percent over the same wavelength range.

An exact comparison between measured and computed albedos can be made by using our $r_\pm$ values as upper boundary conditions in the direct irradiance model of Preisendorfer and Mobley (1984). This model may be solved to find the upward irradiance just below the water surface. From this and our $t_+ = 1 - r_+$ values, the transmitted irradiance just above the surface can be determined. However, the solution of the irradiance equations requires knowing the absorption and backscatter coefficients of the water, and these quantities are not documented in the empirical studies.

Both Payne, and Simpson and Paulson parameterized the sky radiance distribution using the atmospheric transmittance, T, which is the ratio of measured downward irradiance to the irradiance which would fall on the earth's surface in the absence of an atmosphere. Values of $T \leqslant 0.1$ correspond to a heavy overcast and $T \geqslant 0.6$ to a clear day; $T = 1$ would correspond to no atmosphere. As noted in Simpson and Paulson, this parameterization is not entirely satisfactory, since different sky conditions (e.g., cloud distribution and haziness) having quite different radiance distributions can have the same T value.

Neither of the empirical studies presents albedos as a function of wind speed, beyond noting that the albedo decreases with increasing wind speed for clear skies and for solar angles corresponding to our θ'_s in the range $60° \leqslant \theta'_s \leqslant 75°$. No wind speed dependence was discernible for $\theta'_s < 60°$. These observations are consistent with our curves of Fig. 16. Neither study could make reliable measurements for sun positions near the horizon ($\theta'_s > 75°$) or for sun positions near the zenith. For clear sky conditions ($0.5 \leqslant T \leqslant 0.6$) and $50° \leqslant \theta'_s \leqslant 60°$, measured albedos are in the range 0.05 to 0.08. As expected, these values are somewhat larger than our computed values of 0.033 to 0.067 (obtained from Fig. 18), which correspond to $T = 1.0$. Payne extrapolates his curves from $T = 0.65$ to $T = 1.0$ and finds albedos in the range of 0.044 at $\theta'_s = 50°$ to 0.065 at $\theta'_s = 60°$. Measured albedos as low as 0.03 are found for clear skies and high sun angles, and albedos as high as 0.5 are found for low sun angles. For heavily overcast skies, measured albedos average about 0.06 in both studies. The average wind speed for Payne's measurements was 3.7 m s^{-1} and for Simpson and Paulson the average was 6 m s^{-1} (anemometer heights not specified). Albedos of 0.06 are consistent with our computed values of r_- for uniform and cardioidal radiance distributions and moderate wind speeds (Fig. 21). Payne remarks that the effects of whitecaps are not noticeable at wind speeds up to 15 m s^{-1}. The reasonable agreement between the computed r_- values and the measured albedos lends support to our model assumption that capillary waves largely determine the optical properties of the sea surface.

Payne also uses his measurements to estimate climatological albedos as functions of latitude and month. By combining our computed r_+ values and the direct solutions of the irradiance model of Preisendorfer and Mobley (1984) with climatological values of wind speed, cloud cover and water type, one could generate a detailed atlas of albedos. The recent availability of comprehensive ocean–atmosphere datasets makes such calculations feasible. However, such a project, worthwhile as it is, is beyond the scope of the present paper.

Acknowledgments. Support of the work by one of us (C.D.M.) was provided in part by Equatorial Pacific Ocean Climate Study Council and the National Climate Program Office. Ryan Whitney provided word processing and editorial assistance. Joy Register and Gini Curl helped prepare the diagrams.

REFERENCES

Cox, C., and W. Munk, 1954a: The measurement of the roughness of the sea surface from photographs of the sun's glitter. *J. Opt. Soc. Amer.*, **44,** 838–850.

——, and ——, 1954b: Statistics of the sea surface derived from sun glitter. *J. Mar. Res.*, **13,** 198–227.

——, and ——, 1955: Some problems in optical oceanography. *J. Mar. Res.*, **14,** 63–78.

Duntley, S. Q., 1950: *The Visibility of Submerged Objects, Part 1. Optical effects of water waves.* MIT, Office of Naval Research Contract N5ori-07831 and Bureau of Ships contract NObs-50378, 11 pp.

——, 1954: Measurements of the distribution of water wave slopes. *J. Opt. Soc. Amer.*, **44,** 574–575.

——, 1963: Light in the sea. *J. Opt. Soc. Amer.*, **53,** 214–233.

——, and R. W. Preisendorfer, 1952: *The Visibility of Submerged Objects.* Final Rep., MIT, Office of Naval Research Contracts N5ori-07831, N5ori-07864 and Bureau of Ships contract NObs-50378, 74 pp.

Eckart, C., 1946: The sea surface and its effect on the reflection of sound and light. File Rep. 01.75, UCDWR M407, Contract NO6s-2079, University of California Division of War Research at the U.S. Navy Electronics Lab., San Diego, 18 pp.

Guinn, J. A., G. N. Plass and G. W. Kattawar, 1979: Sunlight glitter on a wind-ruffled sea: Further studies. *Appl. Opt.*, **18,** 842–849.

Hulburt, E. O., 1934: The polarization of light at sea. *J. Opt. Soc. Amer.*, **24,** 35–42.

Neumann, G., 1953: *On Ocean Wave Spectra and a New Method of Forecasting Wind-Generated Sea.* Beach Erosion Board, Corps of Engineers, Tech. Memo. 43, 42 pp.

Payne, R. E., 1972: Albedo of the sea surface. *J. Atmos. Sci.*, **29,** 959–970.

Pierson, W. J., 1955: Wind generated gravity waves. *Advances in Geophysics,* Vol. 2, Academic Press, 93–178.

——, and W. Marks, 1952. The power spectrum analysis of ocean-wave records. *Trans. Amer. Geophys. Union.*, **33,** 834–844.

Preisendorfer, R. W., 1965: *Radiative Transfer on Discrete Spaces.* Pergamon, 462 pp.

——, 1971: General theory of radiative transfer across the random atmosphere–ocean interface. *J. Quant. Spectrosc. Radiat. Transfer,* **11,** 723–737.

——, 1976: *Hydrologic Optics.* Pacific Marine Environmental Laboratory, ERL/NOAA, 1757 pp. [A six volume set: Vol. I, *Introduction,* PB-259793/8ST; Vol. II, *Foundations,* PB-259794/6ST; Vol. III, *Solutions,* PB-259795/3ST; Vol. IV, Imbeddings, PB-259796/1ST; Vol. V, *Properties,* PB-259797/9ST; Vol. VI, *Surfaces,* PB-268704/4ST.]

——, and C. D. Mobley, 1984: Direct and inverse irradiance models in hydrologic optics. *Limnol. Oceanogr.*, **29,** 903–929.

——, and ——, 1985: Unpolarized irradiance reflectance of random capillary waves on lakes and seas, by Monte Carlo simulation. NOAA Tech. Memo. ERL PMEL-63, 141 pp.

Schooley, A. H., 1954: A simple optical method of measuring the statistical distribution of water surface slopes. *J. Opt. Soc. Amer.*, **44,** 37–40.

Shuleikin, V. V., 1968: *Fizika Moria* (*Physics of the Sea*). 4th Ed. revised and expanded, *Izd. Akad. Nauk SSSR.*

Simpson, J. J., and C. A. Paulson, 1979. Mid-ocean observations of atmospheric radiation. *Quart. J. Roy. Meteor. Soc.*, **105,** 487–502.

Reprinted from JOURNAL OF PHYSICAL OCEANOGRAPHY, Vol. 17, No. 4, April 1987
American Meteorological Society

Reply

CURTIS D. MOBLEY AND RUDOLPH W. PREISENDORFER*

NOAA/ERL/Pacific Marine Environmental Laboratory, Seattle, WA 98115

4 October 1986

We explicitly noted in paragraph 4, section 9 of our paper that we expected our results to be in error by some unknown amount if whitecaps were present at higher wind speeds. We considered including the statement that, in the presence of whitecaps, the albedo of the sea surface, r_-, would be given by

$$r_- = r_-(\text{water}) \cdot (1 - f) + r_-(\text{foam}) \cdot f,$$

where f is the fraction of the sea surface covered by whitecaps, $0 \leq f \leq 1$, r_- (water) is the albedo of the water, and r_- (foam) is the albedo of the foam in the whitecaps. However, we did not have available data of the quality shown in Fig. 1 of the comments, from which we could have determined f. Moreover, even if f is known, there is considerable uncertainty in the value of r_- (foam): values cited in the comments range from 0.22 to 0.6. Thus, we felt it beyond the scope of our paper to discuss the effects of whitecaps in any detail.

We reiterate that there are still other physical processes which can affect the albedos, but which are not considered in our surface study. In particular, the optical properties of the water body itself can alter the albedo r_- (water) by perhaps as much as 10%, as we noted in our section 10. In optically shallow water (e.g., nearshore coastal regions or lakes) bottom characteristics also influence this albedo. Both of these effects can be accounted for by using the irradiance model referenced in our paper together with the results of the surface study.

Our calculations of the contribution of the water surface to the total albedo stand complete and correct for the stated model. The work of Monahan and O'Muircheartaigh is a welcome extension of our study and complements our estimates of the sea surface albedos.

* Deceased.